



The Physical Properties of Star-forming Galaxies with Strong [O III] Lines at $z = 3.25$

Run Wen^{1,2} , Fangxia An³ , Xian Zhong Zheng^{1,2} , Dong Dong Shi¹ , Jianbo Qin¹ , Valentino Gonzalez^{4,5} , Fuyan Bian⁶ , Haiguang Xu⁷ , Zhizheng Pan¹ , Qing-Hua Tan¹ , Wenhao Liu¹, Min Fang¹, Jian Ren^{1,2}, Yu Heng Zhang^{1,2}, Man Qiao^{1,2}, and Shuang Liu^{1,2}

¹ Purple Mountain Observatory, Chinese Academy of Sciences, 10 Yuanhua Road, Qixia District, Nanjing 210023, People's Republic of China; xzzheng@pmo.ac.cn

² School of Astronomy and Space Sciences, University of Science and Technology of China, Hefei 230026, People's Republic of China

³ Inter-University Institute for Data Intensive Astronomy, and Department of Physics and Astronomy, University of the Western Cape, Robert Sobukwe Road, 7535 Bellville, Cape Town, South Africa

⁴ Chinese Academy of Sciences South America Center for Astronomy, China-Chile Joint Center for Astronomy, Camino del Observatorio 1515, Las Condes, Chile

⁵ Centro de Astrofísica y Tecnologías Afines (CATA), Camino del Observatorio 1515, Las Condes, Santiago, Chile

⁶ European South Observatory, Alonso de Cordova 3107, Casilla 19001, Vitacura, Santiago 19, Chile

⁷ School of Physics and Astronomy, Shanghai Jiao Tong University, 800 Dongchuan Road, Shanghai 200240, People's Republic of China

Received 2022 March 1; revised 2022 May 22; accepted 2022 May 24; published 2022 July 4

Abstract

We present an analysis of physical properties of 34 [O III] emission-line galaxies (ELGs) at $z = 3.254 \pm 0.029$ in the Extended Chandra Deep Field South (ECDFS). These ELGs are selected from deep narrow $H_2S(1)$ and broad K_s imaging of 383 arcmin^2 obtained with CFHT/WIRCam. We construct spectral energy distributions (SEDs) from U to K_s to derive the physical properties of ELGs. These [O III] ELGs are identified as starburst galaxies with strong [O III] lines of $L_{\text{OIII}} \sim 10^{42.6} - 10^{44.2} \text{ erg s}^{-1}$ and have stellar masses of $M_* \sim 10^{9.0} - 10^{10.6} M_\odot$ and star formation rates of $\sim 10 - 210 M_\odot \text{ yr}^{-1}$. Our results show that 24% of our sample galaxies are dusty with $A_V > 1 \text{ mag}$ and $\text{EW}([\text{O III}])_{\text{rest}} \sim 70 - 500 \text{ \AA}$, which are often missed in optically selected [O III] ELG samples. Their rest-frame UV and optical morphologies from HST/ACS and HST/WFC3 deep imaging reveal that these [O III] ELGs are mostly multiple-component systems (likely mergers) or compact. And 20% of them are nearly invisible in the rest-frame UV owing to heavy dust attenuation. Interestingly, we find that our sample ELGs reside in an overdensity consisting of two components: one southeast (SE) with an overdensity factor of $\delta_{\text{gal}} \sim 41$ over a volume of 13^3 cMpc^3 , and the other northwest (NW) with $\delta_{\text{gal}} \sim 38$ over a volume of 10^3 cMpc^3 . The two overdense substructures are expected to be virialized at $z = 0$ with a total mass of $\sim 1.1 \times 10^{15} M_\odot$ and $\sim 4.8 \times 10^{14} M_\odot$ and probably merge into a Coma-like galaxy cluster.

Unified Astronomy Thesaurus concepts: [Galaxy formation \(595\)](#); [Galaxy evolution \(594\)](#); [High-redshift galaxies \(734\)](#)

1. Introduction

The past two decades have witnessed a wealth of progress in mapping galaxy formation and evolution. The current generation of multiwavelength deep surveys have revealed the detailed properties of galaxy populations out to $z \sim 2 - 3$, where the cosmic star formation rate density (CSFRD) reaches its peak (Hopkins & Beacom 2006; Sobral et al. 2013; Madau & Dickinson 2014; Khostovan et al. 2015). At $z > 2 - 3$ about one-quarter of the present-day stars were formed in the progenitors of present-day massive galaxies (Madau & Dickinson 2014), preferentially in the overdense environments (Thomas et al. 2005; Chiang et al. 2017). Characterizing the properties of galaxies at $z > 3$ is thus essential to understanding the early formation of massive galaxies and large-scale structures, as well as how the star formation activities are activated to reach the peak of CSFRD (Suzuki et al. 2015; Onodera et al. 2016, 2020).

The emission lines in the rest-frame optical spectra of galaxies (e.g., [O II] $\lambda\lambda 3727, 3729, H\beta$, [O III] $\lambda\lambda 4959, 5007$, [N II] $\lambda\lambda 6549, 6585, H\alpha$ and [S II] $\lambda\lambda 6718, 6732$) are mostly used for physical and chemical diagnostics (see Kewley et al. 2019, for a review). Moreover, studies of emission-line

galaxies (ELGs) at $z > 3$ provide insights into understanding the cosmic reionization (de Barros et al. 2016). The universe is fully ionized by $z \sim 6$ (e.g., Fan et al. 2006; de Barros et al. 2014). Star-forming galaxies (SFGs) at $z > 6$ are thought to be the main contributors to the ionizing field in the era of reionization (e.g., Nakajima & Ouchi 2014; Robertson et al. 2015). Owing to the opaque intergalactic medium (e.g., Worseck et al. 2014), the nature of ionizing sources in the reionization era is still not well understood.

These ionizing sources usually have prominent [O III]+H β emission (De Barros et al. 2019; Endsley et al. 2021). The strong [O III] emission lines may reveal the extreme conditions of the interstellar medium in a galaxy and likely are associated with low metallicity and high ionizing parameters (McLinden et al. 2011; Nakajima & Ouchi 2014; Onodera et al. 2020; Tang et al. 2021b). The extreme [O III] ELGs are often seen as analogs of galaxies in the reionization era (Tang et al. 2019; Du et al. 2020; Tang et al. 2021a, 2022). And galaxies with large [O III] equivalent widths (EWs; from 200 to 800 Å) are widely used to address the Ly α continuum escape fraction in the high- z universe (Fletcher et al. 2019; Barrow et al. 2020; Katz et al. 2020; Nakajima et al. 2020). Their analogs at low z refer to the so-called “Green Pea” galaxies (Cardamone et al. 2009), showing strong [O III] emission with extremely high [O III]/[O II] ratio (Jaskot & Oey 2013; Yang et al. 2017; Yuma et al. 2019; Lumberras-Calle et al. 2021; Liu et al. 2022). The [O III] lines redshift into the near-infrared (NIR) and mid-infrared

(MIR) bands for $z > 3$ objects. Deep IR photometric and spectroscopic observations are thus crucial to identifying and studying SFGs at $z > 3$ (e.g., Bunker et al. 1995; Geach et al. 2008; Nakajima et al. 2013; Sobral et al. 2013; Khostovan et al. 2016).

However, the NIR observations of high- z galaxies can be carried out only in the J , H , and K_s bands on the ground owing to the atmospheric transmission. And the high sky background leads such observations to be very time-consuming and available only for a limited sky area. MOSFIRE on board the Keck telescope is an efficient instrument in taking NIR spectroscopy of high- z galaxies (McLean et al. 2012). The NIR spectroscopic surveys with MOSFIRE, e.g., the Keck Baryonic Structure Survey (KBSS-MOSFIRE; Steidel et al. 2014) and the MOSFIRE Deep Evolution Field survey (MOSDEF; Kriek et al. 2015; Shapley et al. 2015; Reddy et al. 2018), obtained rest-frame optical spectra of thousands of galaxies mostly at $z \sim 1.4$ – 3 based on the H -band selection. In contrast, the NIR observations with space-borne facilities are free from the atmospheric emission but constrained by the thermal emission from the facilities. The IR grism surveys using WFC3 on board the Hubble Space Telescope (HST), e.g., the WFC3 Infrared Spectroscopic Parallel Survey (WISP; Atek et al. 2011), the MAMMOTH-Grism HST slitless spectroscopic survey (Wang et al. 2022), and the 3D-HST survey (Brammer et al. 2012; Momcheva et al. 2016), provided low-resolution rest-frame optical spectra for a large number of galaxies out to $z \sim 2.5$. These NIR surveys have built a more comprehensive view of the physical properties of galaxies at $1 < z < 3$. The James Webb Space Telescope (JWST) will offer unprecedented sensitivities in the NIR and MIR to conduct imaging and spectroscopy of high- z galaxies and revolutionize our understanding of galaxy formation and evolution since the era of reionization.

Deep imaging through narrow- and broadband K_s enables us to detect the emission lines [O III] $\lambda\lambda 4959, 5007$ in galaxies over $3 < z < 3.7$ and even determine the [O III] luminosity functions (Reddy et al. 2008; Kashikawa et al. 2011; Khostovan et al. 2015; Sobral et al. 2015; Gong et al. 2017; Khostovan et al. 2020). Such observations are often used to identify $H\alpha$ and other emission lines at lower redshifts (Khostovan et al. 2015, 2016). It has been verified that the approach with NIR narrowband imaging is effective in probing ELGs within a narrow redshift range of $\delta z / (1 + z) = 1\%$ – 2% over a large sky coverage (Sobral et al. 2013). On the other hand, the presence of strong [O III] emission lines may cause an excess of the observed K_s flux relative to the continuum flux derived from broadband spectral energy distributions (SEDs) and be used to identify [O III] ELGs at $3 < z < 3.7$ (Onodera et al. 2020). Pilot studies of [O III] ELGs with spectroscopic observations have contributed to addressing the kinematic and structural evolution of [O III] SFGs (Steidel et al. 2010; McLinden et al. 2013; Schenker et al. 2013; Gillman et al. 2019; Price et al. 2020; Tran et al. 2020; Yates et al. 2020), as well as metal enrichments (e.g., Kewley & Ellison 2008; Mannucci et al. 2010; Sommariva et al. 2012; Nakajima & Ouchi 2014; Troncoso et al. 2014; Nakajima et al. 2016).

In the Extended Chandra Deep Field South (ECDFS), a deep narrowband imaging survey has been carried out with CFHT/WIRCam, detecting a sample of 34 [O III] ELGs at $z \sim 3.25$ (An et al. 2014, hereafter A14). Here we conduct a detailed analysis of the physical properties of these [O III] ELGs using

the publicly available multiwavelength data. This paper is organized as follows: In Section 2, we briefly introduce our narrowband imaging observations and multiwavelength data used in our analysis. Section 3 displays the input parameters of SED fitting and gives the results. We present the physical properties of our [O III] samples in Section 4, and the overdensity in ECDFS traced by [O III] is shown in Section 5. We discuss our results in Section 6. In Section 7 we give a summary of this work. Throughout this paper we adopt cosmological parameters of $\Omega_M = 0.3$, $\Omega_\Lambda = 0.7$, and $H_0 = 70 \text{ km s}^{-1} \text{ Mpc}^{-1}$. Unless otherwise stated, all magnitudes are given in the AB magnitude system (Oke 1974), and a Chabrier initial mass function (IMF; Chabrier 2003) is assumed.

2. Sample and Data

A14 presented the observations and detections of 140 emission-line objects with the $H_2S(1)$ narrowband and K_s broadband imaging of ECDFS. Of the 140 objects, 34 are recognized as [O III] ELGs at $z \sim 3.25$. Here we briefly describe the NIR observations, data, and selection for the sample of 34 [O III] ELGs. More details can be found in A14.

2.1. Sample Selection

A deep imaging survey of ECDFS (centered at $\alpha = 03:28:45$, $\delta = -27:48:00$) was conducted through the narrowband filter $H_2S(1)$ ($\lambda_c = 2.130 \mu\text{m}$, $\Delta\lambda = 0.0293 \mu\text{m}$) with the instrument WIRCam on board the Canada–France–Hawaii Telescope (CFHT; Puget et al. 2004). WIRCam consists of four 2048×2048 HAWAII2-RG detectors, providing a sky coverage of $20' \times 20'$ with a pixel scale of $0''.3 \text{ pixel}^{-1}$. The deep K_s -band ($\lambda_c = 2.146 \mu\text{m}$, $\Delta\lambda = 0.325 \mu\text{m}$) imaging data were also obtained with CFHT/WIRCam and adopted in our analysis from Hsieh et al. (2012). The final science images reach a 5σ depth of $H_2S(1) = 22.8 \text{ mag}$ and $K_s = 24.8 \text{ mag}$ for point sources.

The $H_2S(1)$ and K_s imaging data of ECDFS are used to identify ELGs with the $K_s - H_2S(1)$ color excess (Bunker et al. 1995) following

$$K_s - H_2S(1) > -2.5 \log(1 - \Sigma \sqrt{\sigma_{K_s}^2 + \sigma_{H_2S(1)}^2} / f_{H_2S(1)}), \quad (1)$$

where Σ is the significant factor and $\sigma_{H_2S(1)}$ and σ_{K_s} are background noises in the two bands. The Σ is introduced to identify ELGs with the combined 1σ photometric error from both the narrow and broad bands. Here $f_{H_2S(1)}$ refers to $H_2S(1)$ flux as $f_{H_2S(1)} = 0.3631 \times 10^{0.4(25 - H_2S(1))}$. The noises and fluxes are given in units of μJy . Using the color excess criteria, in total 8720 sources were detected with $S/N > 5$ in both $H_2S(1)$ and K_s . Their fluxes were measured from the corresponding images using the software tool SExtractor (Bertin & Arnouts 1996). With the selection criteria of $\Sigma = 3$ and $EW > 50 \text{ \AA}$, in total 140 objects were securely selected as emission-line candidates.

2.2. Public Data

We utilize optical U -, B -, V -, R -, and I -band photometric catalog and imaging data from the Multiwavelength Survey by Yale-Chile (MUSYC; Gawiser et al. 2006; Cardamone et al. 2010); HST/ACS F606W (V_{606}) and F850LP (z_{850}) imaging

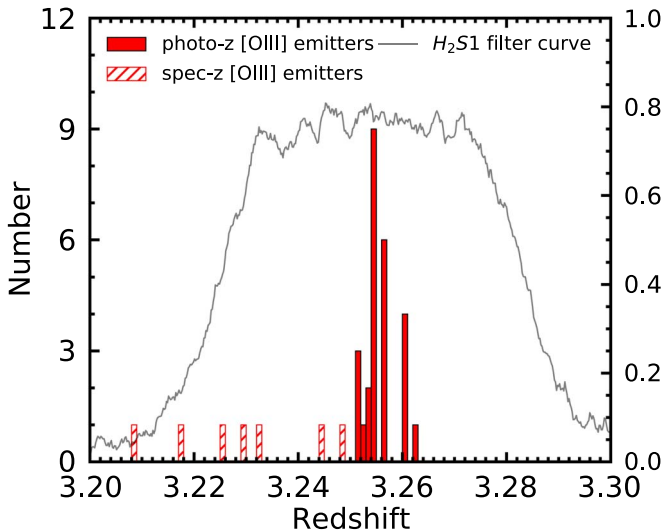


Figure 1. Redshift distribution of 34 [O III] ELGs. A bin width of 0.001 is adopted. The filled histogram presents the distribution of [O III] ELGs with photo- z , while the hatched histogram refers to spec- z . The gray curve is the width range of $H_2S(1)$ filter for the [O III] $\lambda 5007$ emission line at $z \sim 3.25$.

from the GEMS survey (Rix et al. 2004; Caldwell et al. 2008); HST/WFC3 F125W (J_{125}) and F160W (H_{160}) imaging from the Cosmic Assembly Near-infrared Deep Extragalactic Legacy Survey (CANDELS; Grogin et al. 2011; Koekemoer et al. 2011); and CFHT/WIRCam J and K_s imaging data (Hsieh et al. 2012), in conjunction with our $H_2S(1)$ imaging data. Fluxes in these 12 bands are obtained for the sample of 140 emission-line candidates. Note that 16 targets are optically too faint to be included in the MUSYC public catalog, and 72 sources out of the 140 candidates have J_{125} and H_{160} data since the CANDELS survey only covers a part of ECFDS.

By fitting their SEDs composed of 12-band data points with the software tool EAZY (Easy and Accurate Redshifts from Yale; Brammer et al. 2008), photometric redshifts (photo- z) were derived for the 140 emission-line candidates (the modeling will be introduced in Section 3). Of them, 34 ELGs with $2.8 < z_{\text{phot}} < 3.3$ are identified as [O III] emitters at $z \sim 3.25$. With the public catalogs available in the literature, we also identify that 8 of these 34 ELGs have spectroscopic redshifts (spec- z). Except for one source that has a spec- z at 3.083, the spec- z of the remaining seven sources is in the range of 3.208–3.248, confirming that these ELGs are located at $z \sim 3.25$.

The redshift distribution of the 34 [O III] ELGs and $H_2S(1)$ width are shown in Figure 1. Because the narrowband filter $H_2S(1)$ has a relatively small bandwidth $\Delta\lambda$, we attribute the emission line detected in this band to [O III] $\lambda 5007$ (this will be discussed later in Section 6.1). More details about emission-line source selection and the EAZY SED fittings can be found in An et al. (2013) and A14.

3. SED Fitting

In order to maximize signal-to-noise ratio (S/N) for aperture-matched colors between the 12 bands mentioned above, A14 first determined colors for MUSYC, HST, and CFHT bands, respectively, and then matched three sets of colors to establish SED input fluxes from U to K_s . Finally, the SED was scaled up to meet the total flux of K_s derived from aperture photometry within a diameter of $2'$ corrected for the

missing flux out of the aperture (see A14 for more details). The photometric fluxes in the 12 bands from U to K_s for our sample of 34 [O III] ELGs are listed in Table 1.

Photometric redshifts (photo- z) were derived from these SEDs using EAZY with relatively small errors partially because of the narrowband data points linked to given redshifts traced by emission lines. The galaxy SED templates were generated from a library of six independent templates in EAZY. This gives a fast determination on photo- z but sacrifices the accuracy in modeling the details of SEDs (e.g., line fluxes). Therefore, we utilize the Code Investigating GALaxy Emission (CIGALE; Boquien et al. 2019) to analyze the SEDs of our [O III] ELGs with the improved galaxy templates. CIGALE produces millions of models to fit the observational data and estimates their physical properties such as stellar mass, star formation rate (SFR), and dust attenuation, while applying a Bayesian statistical analysis approach to estimate the results. The photo- z obtained with EAZY are used in the CIGALE fitting as the input redshift since CIGALE is not optimized to measure photometric redshift.

The Chabrier (2003) IMF and the stellar population synthesis model from Bruzual & Charlot (2003) are adopted for the fitting. We set three values of metallicity as 0.0004, 0.008, and 0.02 (for $Z_{\odot} = 0.02$) in stellar models. A delayed form of star formation history (SFH), $\text{SFR} \propto t/\tau_{\text{main}}^2 \exp(-t/\tau_{\text{main}})$, is adopted in our fitting too, where t is the time of the star formation onset and τ_{main} is the e -folding time of the main stellar population. Such a functional form is more physical than a simple exponential SFH because it removes the discontinuity in SFR at $t = 0$ and is able to produce an increasing SFR when τ is large (Carnall et al. 2019). A starburst component f_{burst} can be added at a given mass fraction as well. This SFH can fit the high- z SFGs well since they usually have a relatively strong star formation activity. It also avoids the systematic biases caused by the degeneracy between the slope of the dust attenuation curve, effective dust attenuation, and intrinsic UV slope of model templates (Yuan et al. 2019; Villa-Vélez et al. 2021; Qin et al. 2022). The degeneracy is indeed smaller for blue SFGs. However, high- z SFGs may have nonnegligible dust attenuation, and this could increase the degeneracy for these dusty objects.

For nebular emission, the initial parameters include the dimensionless ionization parameter $\log U$, the escape fraction of Lyman continuum photons f_{esc} , and the fraction of Lyman continuum photons absorbed by dust f_{dust} . The radiation strength U is set to be -2.0 , while f_{esc} and f_{dust} have values of 0.0, 0.1, and 0.2.

We adopt the modified Calzetti law (Calzetti et al. 2000; Noll et al. 2009) to describe the dust attenuation in our fitting. The attenuation for nebular emission is higher than that for stellar emission. We set $E(B-V)_{\text{factor}}$, a ratio of $E(B-V)_{\text{star}}$ to $E(B-V)_{\text{gas}}$, to be 0.44 (Calzetti et al. 2000). Meanwhile, the color excess of the nebular lines $E(B-V)_{\text{gas}}$ and the slope of the power law modifying the attenuation curve δ are chosen to change freely, in the range of 0.05–0.8 and -1.0 to 0.2, respectively. We also take the amplitude of UV bump to be 0, 1, 2, 3, or 4, where 3 corresponds to the value of the Milky Way. And the ratio of total to selective extinction R_V is fixed to a standard value of 3.1.

Due to the lack of detections in the far-IR, the SED of dust emission is not well constrained in our work. The dust emission is modeled with templates from Dale et al. (2014), which

Table 1
Multiband Photometry of 34 [O III] Emitters of Our Samples

ID	R.A.(J2000)	Decl.(J2000)	f_U	f_B	f_V	f_R	f_I	f_{606}	f_{850}	f_{125}	f_{160}	f_J	$f_{H2S(1)}$	K_s
1	53.176239	-27.978130	-0.15 ± 0.02	0.20 ± 0.01	0.38 ± 0.02	0.53 ± 0.11	0.54 ± 0.02	0.45 ± 0.01	0.70 ± 0.05	0.69 ± 0.07	2.60 ± 0.41	1.23 ± 0.11
2	53.159058	-27.972429	-0.13 ± 0.02	0.18 ± 0.01	0.32 ± 0.02	0.44 ± 0.10	0.49 ± 0.02	0.40 ± 0.01	0.62 ± 0.04	0.80 ± 0.06	4.14 ± 0.33	1.69 ± 0.09
3	53.178284	-27.969770	-0.17 ± 0.02	0.39 ± 0.02	0.65 ± 0.02	0.98 ± 0.12	0.84 ± 0.02	0.74 ± 0.02	0.93 ± 0.05	1.00 ± 0.10	6.93 ± 0.47	2.06 ± 0.14
4	53.239136	-27.951475	-0.20 ± 0.03	0.15 ± 0.02	0.30 ± 0.02	0.47 ± 0.14	0.46 ± 0.02	0.38 ± 0.02	0.46 ± 0.06	0.49 ± 0.08	3.09 ± 0.46	1.20 ± 0.12
5	53.158218	-27.950077	-0.10 ± 0.01	0.36 ± 0.01	0.65 ± 0.01	1.30 ± 0.08	0.99 ± 0.01	...	0.59 ± 0.03	1.39 ± 0.07	5.81 ± 0.28	2.97 ± 0.11
6	52.965435	-27.948175	-0.14 ± 0.02	0.17 ± 0.01	0.31 ± 0.02	0.54 ± 0.11	0.40 ± 0.02	0.36 ± 0.01	0.42 ± 0.04	0.61 ± 0.06	5.61 ± 0.27	1.32 ± 0.09
7	53.173649	-27.943214	-0.10 ± 0.01	-0.06 ± 0.01	0.10 ± 0.01	-0.41 ± 0.07	0.17 ± 0.01	...	0.29 ± 0.03	0.20 ± 0.05	2.65 ± 0.22	0.70 ± 0.07
8	53.162315	-27.942719	-0.10 ± 0.01	0.17 ± 0.01	0.32 ± 0.01	0.65 ± 0.08	0.45 ± 0.01	...	0.59 ± 0.03	1.12 ± 0.05	4.57 ± 0.24	1.79 ± 0.08
9	53.171169	-27.932827	-0.17 ± 0.03	0.11 ± 0.02	0.27 ± 0.02	-0.72 ± 0.13	0.34 ± 0.02	0.30 ± 0.00	0.67 ± 0.01	0.48 ± 0.02	0.79 ± 0.02	0.38 ± 0.06	2.97 ± 0.37	0.97 ± 0.09
10	53.170116	-27.929638	0.17 ± 0.01	0.36 ± 0.02	1.07 ± 0.02	2.24 ± 0.02	0.95 ± 0.05	26.41 ± 0.28	8.25 ± 0.08
11	53.161907	-27.920698	-0.12 ± 0.02	0.08 ± 0.01	0.13 ± 0.02	-0.50 ± 0.09	0.18 ± 0.01	0.15 ± 0.01	0.19 ± 0.02	0.16 ± 0.01	0.20 ± 0.02	0.21 ± 0.05	2.19 ± 0.26	0.62 ± 0.07
12	53.167480	-27.913368	-0.12 ± 0.02	-0.07 ± 0.01	-0.09 ± 0.02	-0.53 ± 0.10	-0.08 ± 0.02	0.18 ± 0.01	0.23 ± 0.01	0.30 ± 0.01	0.44 ± 0.02	0.18 ± 0.05	3.14 ± 0.28	0.85 ± 0.07
13	53.054432	-27.902388	-0.09 ± 0.02	0.21 ± 0.01	0.53 ± 0.01	-0.39 ± 0.08	0.35 ± 0.01	0.43 ± 0.01	0.31 ± 0.03	0.39 ± 0.05	9.06 ± 0.22	1.85 ± 0.07
14	53.148323	-27.901218	-0.18 ± 0.03	0.24 ± 0.02	0.39 ± 0.02	0.46 ± 0.14	0.47 ± 0.02	0.43 ± 0.01	0.56 ± 0.02	0.58 ± 0.02	0.76 ± 0.03	0.68 ± 0.08	3.51 ± 0.45	1.23 ± 0.13
15	53.161755	-27.897072	-0.26 ± 0.02	0.68 ± 0.04	1.13 ± 0.04	1.75 ± 0.16	1.23 ± 0.07	1.18 ± 0.02	1.61 ± 0.04	1.65 ± 0.03	1.97 ± 0.04	1.59 ± 0.15	7.15 ± 0.70	2.61 ± 0.23
16	53.204742	-27.894541	-0.16 ± 0.03	-0.09 ± 0.02	0.16 ± 0.02	-0.66 ± 0.12	0.24 ± 0.02	0.19 ± 0.01	0.31 ± 0.02	0.32 ± 0.02	0.46 ± 0.02	0.34 ± 0.06	2.46 ± 0.36	0.84 ± 0.10
17	53.109936	-27.880537	-0.15 ± 0.02	0.09 ± 0.02	0.16 ± 0.02	-0.64 ± 0.12	0.34 ± 0.02	0.24 ± 0.01	0.39 ± 0.02	0.44 ± 0.07	2.86 ± 0.35	1.16 ± 0.10
18	53.171844	-27.872406	-0.17 ± 0.02	0.17 ± 0.02	0.35 ± 0.02	-0.70 ± 0.13	0.40 ± 0.02	0.37 ± 0.01	0.45 ± 0.02	0.38 ± 0.02	0.45 ± 0.03	0.44 ± 0.08	3.67 ± 0.40	0.93 ± 0.11
19	53.157902	-27.869659	-0.28 ± 0.04	0.54 ± 0.03	0.77 ± 0.03	1.44 ± 0.20	1.03 ± 0.03	0.89 ± 0.02	0.70 ± 0.03	0.84 ± 0.04	1.47 ± 0.04	0.75 ± 0.13	4.27 ± 0.67	1.55 ± 0.21
20	53.048820	-27.865334	-0.27 ± 0.04	-0.16 ± 0.03	-0.19 ± 0.04	-1.14 ± 0.21	-0.17 ± 0.03	0.07 ± 0.02	0.26 ± 0.08	0.38 ± 0.05	0.80 ± 0.06	0.50 ± 0.12	3.30 ± 0.65	1.54 ± 0.17
21	53.019222	-27.847075	-0.10 ± 0.02	-0.06 ± 0.01	0.09 ± 0.01	-0.44 ± 0.08	0.18 ± 0.01	0.13 ± 0.01	0.24 ± 0.03	0.46 ± 0.04	3.31 ± 0.24	1.54 ± 0.07
22	53.061619	-27.846251	-0.20 ± 0.03	0.72 ± 0.02	1.24 ± 0.03	1.26 ± 0.15	1.30 ± 0.02	1.27 ± 0.01	1.39 ± 0.03	1.11 ± 0.02	1.29 ± 0.03	0.98 ± 0.15	4.36 ± 0.61	1.91 ± 0.18
23	53.124718	-27.824574	-0.15 ± 0.02	0.42 ± 0.01	0.77 ± 0.02	0.94 ± 0.11	0.93 ± 0.02	0.85 ± 0.01	1.17 ± 0.02	1.11 ± 0.01	1.39 ± 0.02	0.99 ± 0.06	6.25 ± 0.39	2.29 ± 0.09
24	53.080879	-27.791168	-0.14 ± 0.02	0.15 ± 0.02	0.36 ± 0.02	0.48 ± 0.12	0.46 ± 0.02	0.41 ± 0.01	0.62 ± 0.02	0.66 ± 0.01	0.88 ± 0.02	0.53 ± 0.05	5.22 ± 0.39	1.57 ± 0.09
25	53.106331	-27.783159	-0.15 ± 0.02	0.14 ± 0.02	0.18 ± 0.02	-0.63 ± 0.12	0.22 ± 0.02	0.20 ± 0.01	0.29 ± 0.02	0.43 ± 0.01	0.62 ± 0.02	0.45 ± 0.05	2.83 ± 0.36	1.16 ± 0.09
26	53.263027	-27.759014	-0.16 ± 0.03	0.26 ± 0.02	0.43 ± 0.02	0.51 ± 0.13	0.60 ± 0.02	0.51 ± 0.01	0.56 ± 0.05	0.50 ± 0.10	4.09 ± 0.40	1.21 ± 0.13
27	53.008801	-27.758272	-0.16 ± 0.03	0.10 ± 0.02	0.19 ± 0.02	-0.69 ± 0.13	0.29 ± 0.02	0.23 ± 0.01	0.31 ± 0.03	0.31 ± 0.07	3.93 ± 0.37	1.42 ± 0.11
28	53.013573	-27.755177	-0.14 ± 0.02	0.39 ± 0.02	0.89 ± 0.02	0.56 ± 0.12	0.66 ± 0.02	0.76 ± 0.01	0.65 ± 0.02	0.66 ± 0.01	0.84 ± 0.02	0.62 ± 0.05	10.49 ± 0.33	2.93 ± 0.08
29	53.110451	-27.754616	-0.12 ± 0.02	-0.07 ± 0.01	-0.09 ± 0.02	-0.53 ± 0.10	-0.08 ± 0.02	0.23 ± 0.01	0.41 ± 0.01	0.52 ± 0.01	0.81 ± 0.01	0.46 ± 0.05	2.91 ± 0.31	1.29 ± 0.08
30	53.140198	-27.751116	-0.18 ± 0.03	0.18 ± 0.02	0.28 ± 0.02	-0.77 ± 0.14	0.32 ± 0.02	0.30 ± 0.01	0.39 ± 0.02	0.29 ± 0.02	0.38 ± 0.02	0.25 ± 0.08	2.57 ± 0.48	0.61 ± 0.13
31	53.131378	-27.745434	-0.19 ± 0.03	0.16 ± 0.02	0.33 ± 0.02	-0.79 ± 0.14	0.41 ± 0.02	0.37 ± 0.01	0.54 ± 0.02	0.56 ± 0.02	0.68 ± 0.02	0.46 ± 0.08	3.65 ± 0.48	1.53 ± 0.12
32	53.124756	-27.744980	-0.15 ± 0.02	0.10 ± 0.02	0.18 ± 0.02	-0.62 ± 0.12	0.26 ± 0.02	0.22 ± 0.01	0.32 ± 0.02	0.24 ± 0.01	0.38 ± 0.02	0.40 ± 0.07	4.13 ± 0.39	1.01 ± 0.11
33	53.214493	-27.739864	0.09 ± 0.02	0.57 ± 0.06	0.62 ± 0.08	6.92 ± 0.36	3.65 ± 0.14
34	53.087608	-27.726042	-0.17 ± 0.05	0.38 ± 0.02	0.52 ± 0.02	0.72 ± 0.14	0.59 ± 0.02	0.55 ± 0.01	0.77 ± 0.02	0.85 ± 0.01	1.04 ± 0.01	0.69 ± 0.06	2.25 ± 0.04	1.08 ± 0.10

Note. Note that all fluxes are given in units of μJy .

Table 2
Input Parameters for SED Fitting with CIGALE (Boquien et al. 2019)

Parameter	Symbol	Value
Stellar Population		
Bruzual & Charlot (2003)		
Initial mass function	IMF	Chabrier (2003)
Metallicity	Z_*	0.0004, 0.008, 0.02
Delayed Star Formation History		
e -folding time of main stellar population (Myr)	τ_{main}	50, 100, 200, 500, 4000, 10000
Age of main stellar population (Myr)	age_{main}	50, 500, 1000, 2000
Age of the late burst (Myr)	$\text{age}_{\text{burst}}$	20, 50
e -folding time of the late burst (Myr)	τ_{burst}	10, 50, 100, 1000, 8000
Mass fraction of the late burst population	f_{burst}	0.01, 0.1, 0.2
Nebular Emission		
Ionization parameter	$\log U$	-2.0
LyC escape fraction	f_{esc}	0.0, 0.1, 0.2
LyC absorbed by dust	f_{dust}	0.0, 0.1, 0.2
Dust attenuation		
Noll et al. (2009)		
Color excess of the nebular lines (Mag)	$E(B-V)_{\text{lines}}$	0.05, 0.1, 0.15, 0.2, 0.25, 0.3, 0.4, 0.5, 0.6, 0.7, 0.8
Nebular-to-continuum ratio	$E(B-V)_{\text{factor}}$	0.44
Amplitude of the UV bump	A_{bump}	0, 1, 2, 3, 4
Slope of the attenuation curve	δ	-1.0, -0.8, -0.6, -0.4, -0.2, 0.0, 0.2
Line emission extinction	R_v	3.1
Dust Emission		
Dale et al. (2014)		
Power-law slope $dU/dM \propto U^\alpha$	α	2.0
AGN Model		
Fritz et al. (2006)		
Ratio of the max to min radii of the dust torus	r_{ratio}	30, 100
Torus optical depth at $9.7 \mu\text{m}$	$\tau_{9.7}$	0.3, 2.0
Density function parameter beta	β	-0.5
Density function parameter gamma	γ	4.0
Opening angle of the dust torus (deg)	θ	100
Viewing angle (deg)	ψ	30.1, 60.1
AGN fraction	f_{frac}	0.0, 0.01, 0.1

refines the PAH emission and also adds an optional active galactic nucleus (AGN) fraction in the modeling. The star-forming component is parameterized by a single parameter α defined as $dM_d(U) \propto U^{-\alpha} dU$, where M_d is the dust mass and U is the radiation field intensity. We set the AGN fraction to be zero, and the slope is fixed at $\alpha = 2$.

As pointed out by Lambrides et al. (2020), the X-ray selection might miss faint AGNs at $z > 2$ because their host galaxies usually have strong star formation activities. As a check, we add detailed AGN models from Fritz et al. (2006) in CIGALE to test our results. The ratio of the maximum to minimum radii of the dust torus is set to be 30 and 100, while the optical depth at $9.7 \mu\text{m}$ is 0.3 and 2. And the AGN fraction has a value of 0, 0.01, and 0.1. All the input parameters of CIGALE fitting are given in Table 2.

The best-fit model from CIGALE is chosen using the least-squares method, and the reduced χ^2 ($\chi_r^2 = \chi^2/(N-1)$) is used as a global indicator to quantify the quality of the fitting. Figure 2 shows the results of CIGALE fitting of 34 [O III] ELGs; their ID, photo- z (spec- z if available), and parameter χ_r^2 of the fittings are shown in each panel. The first panel consists of 20 [O III] ELGs with J_{125} and H_{160} imaging data, while the second panel consists of the remaining 14 [O III] ELGs without these two bands. Only one object (ID = 10) shows a large

$\chi_r^2 > 5$ owing to the detection upper limits in five MUSYC bands. About 65% of the objects have $\chi_r^2 < 1$ and 85% have $\chi_r^2 < 3$, suggesting that most of our best-fit SEDs are obtained in good quality.

Note that the 2175 Å bump is present in the best-fit SEDs for some [O III] ELGs in our sample (e.g., ID = 5, 13). We will further examine in Section 4.5 whether such a feature is caused by measurement uncertainties or a solid detection of the 2175 Å bump in $z \sim 3.25$ [O III] ELGs.

4. Properties of [O III] Emission-line Galaxies

4.1. X-Ray Detection

AGN activities can also make a contribution to the [O III] line. Thus, it is essential to verify whether the [O III] emission lines in some of our sample galaxies are powered by AGNs. We first match the X-ray source catalog of 7 Ms Chandra observations in CDFS from Luo et al. (2017) with our sample of [O III] ELGs to examine their X-ray properties. Of the 34 [O III] ELGs, only one object is identified as an X-ray source (XID = 760) in the 7 Ms catalog. Its absorption-corrected intrinsic 0.5–7.0 keV luminosity is $1.12 \times 10^{45} \text{ erg s}^{-1}$. Moreover, this object has the highest [O III] luminosity $L_{\text{OIII}} = 10^{44.2} \text{ erg s}^{-1}$, as well as highest stellar

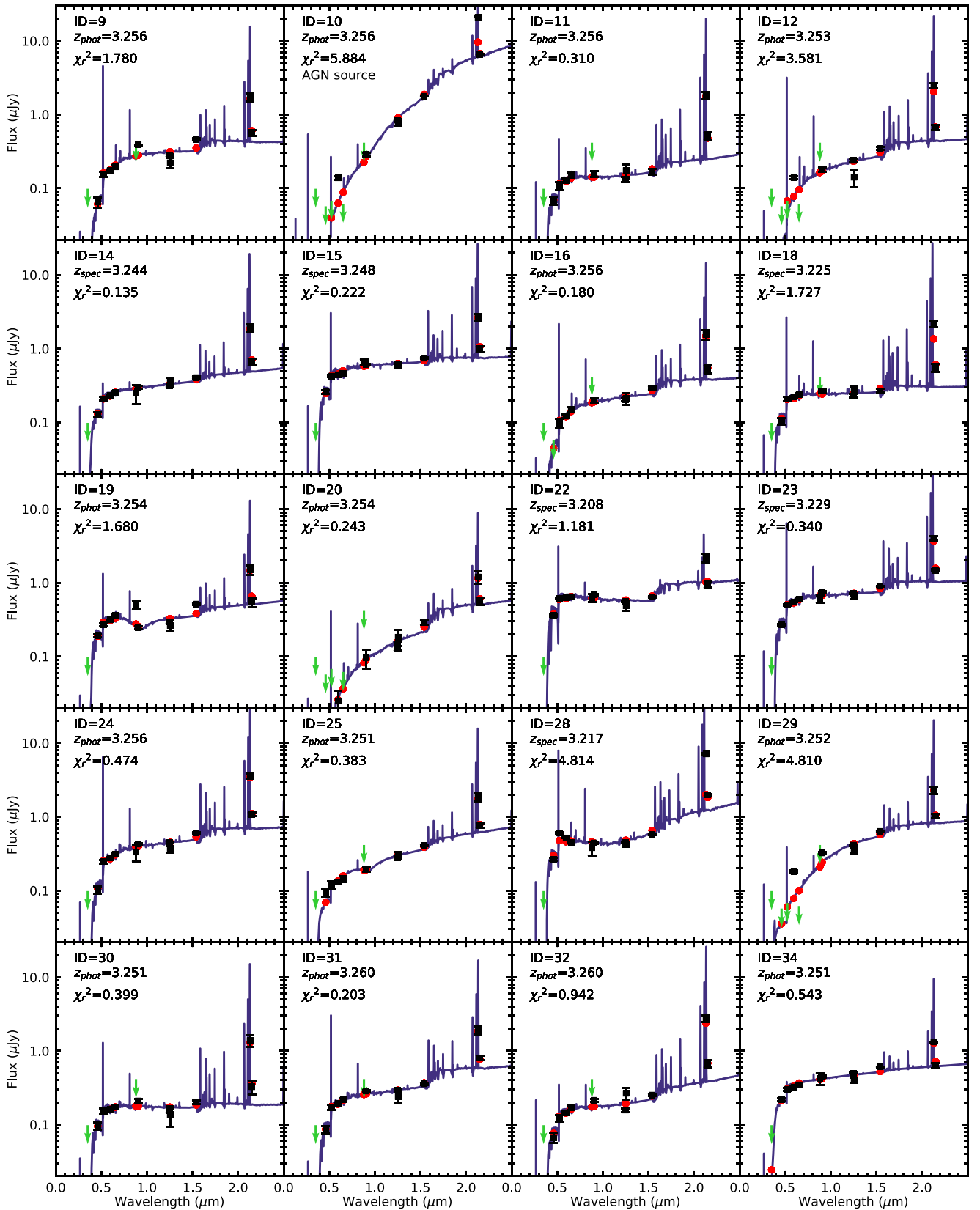


Figure 2. (a) Best-fit SEDs from CIGALE for our sample of 34 $z \sim 3.25$ [O III] ELGs. Black squares and error bars present the observed data points of multiband photometry. Green arrows mark the upper limits of given band detections. Blue lines are the best-fit model SEDs, and red circles refer to the model points in the same bands. The ID, photo- z (spec- z if available), and χ_r^2 are labeled in each panel. The object with ID = 10 hosts an AGN detected in the 7 Ms Chandra observations. These 20 [O III] ELGs have HST/WFC3 J_{125} and H_{160} imaging data. (b) Continued for the best-fit SEDs from CIGALE fitting of the remaining 14 [O III] ELGs, which are not covered by the HST/WFC3 J_{125} and H_{160} imaging.

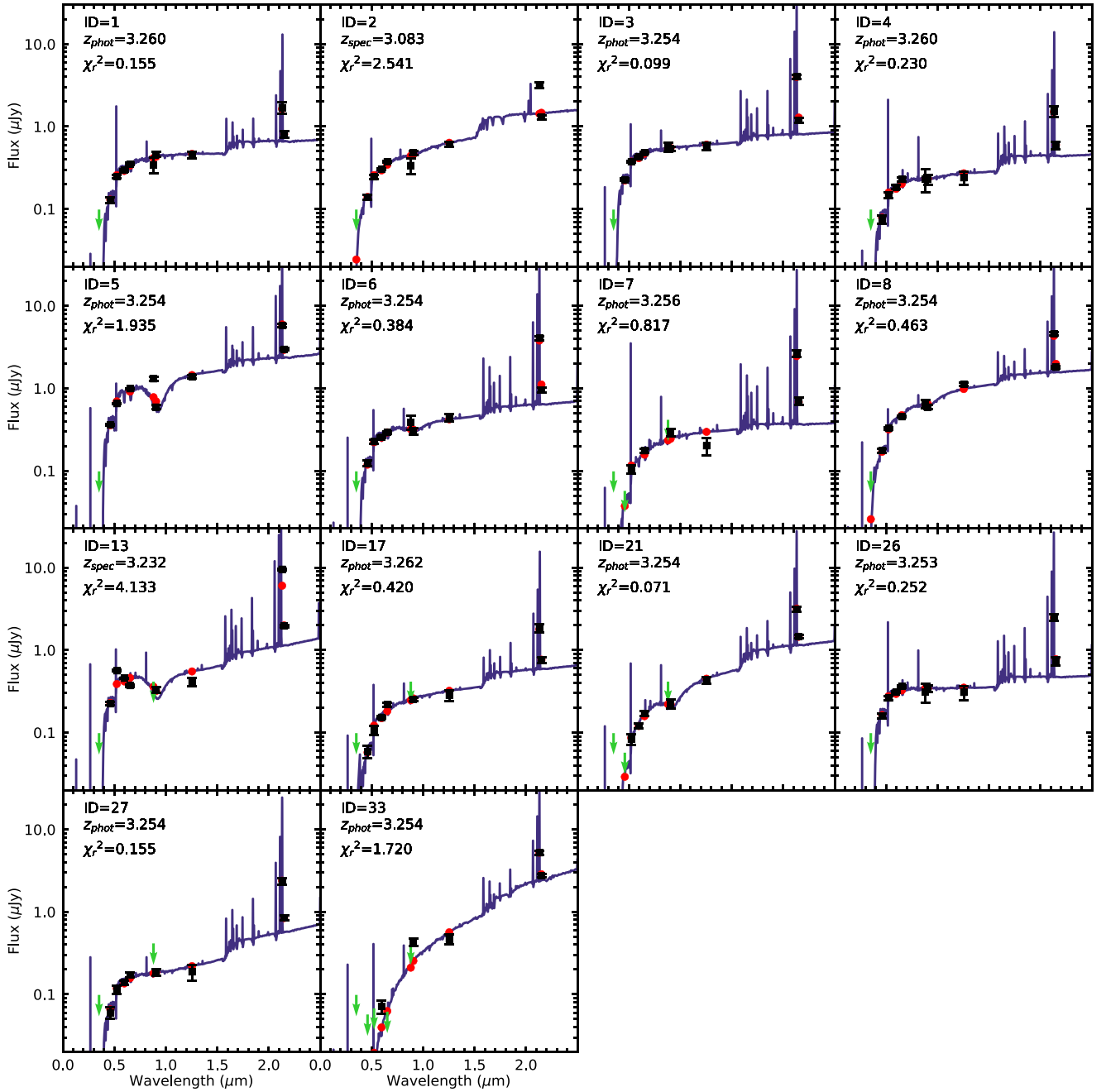


Figure 2. (Continued.)

mass $M_* = 10^{11.4} M_\odot$ (see Table 3). No other X-ray counterparts are found in the 7 Ms catalog for the remaining [O III] ELGs in our sample. The CIGALE results also show that the majority of our [O III] ELGs contain no or a negligible AGN component. Including the X-ray source, six sample galaxies in our sample have an AGN fraction of 0.1, while about half have no AGN fraction in the fitting.

4.2. Morphologies

We use HST/ACS V_{606} and z_{850} imaging data from the GOODS and GEMS surveys to investigate the morphologies of our sample galaxies. For $z \sim 3.25$, these two bands correspond to the rest-frame far-UV (FUV; 1402 Å) and near-UV (NUV; 2130 Å). Note that three [O III] ELGs do not have V_{606} imaging

data owing to the incomplete coverage of the GEMS observations. We adopt the HST/ACS F814W (I_{814}) imaging data to replace V_{606} for making color images of these three objects.

Figure 3 shows the color images made with V_{606} and z_{850} for our [O III] ELGs. A variety of morphologies can be seen. Here we define five morphological types in terms of the compactness and numbers of components of a galaxy. We assign the types of UV faint, compact, diffuse (including clumpy and tidal ones), merging, and multiple component with type ID 1–5, respectively. The morphological types of these 34 [O III] ELGs are visually classified by three of us (R.W., J.R., and S.L.). The median of three classifications is adopted for each galaxy, and the results are presented in Table 3.

Table 3
Physical Properties of 34 Sample [O III] Emitters

ID	z_{phot}	z_{spec}	T^{a}	$U - V^{\text{b}}$ (mag)	$V - J^{\text{c}}$ (mag)	$\text{EW}_{[\text{O III}]}^{\text{rest}}$ (Å)	$\log M_{\text{*}}$ (M_{\odot})	$\log \text{SFR}$ ($M_{\odot} \text{ yr}^{-1}$)	β	A_{FUV} (mag)	A_{V} (mag)	$\log L_{\text{OIII}}$ (erg s^{-1})
1	3.260	...	3	0.36	0.32	94.64 ± 36.60	9.43 ± 0.37	1.40 ± 0.32	-0.48 ± 0.29	1.57 ± 0.35	0.49 ± 0.27	42.77 ± 0.13
2	3.256	3.083	3	0.70	0.54	133.52 ± 25.26	10.03 ± 0.28	1.52 ± 0.44	-0.40 ± 0.31	2.22 ± 0.56	0.67 ± 0.43	43.09 ± 0.06
3	3.254	...	4	0.46	0.07	233.71 ± 41.70	9.48 ± 0.39	1.71 ± 0.27	-0.24 ± 0.26	1.67 ± 0.47	0.74 ± 0.38	43.45 ± 0.04
4	3.260	...	5	0.51	0.21	141.08 ± 49.01	9.35 ± 0.40	1.29 ± 0.37	-0.35 ± 0.29	1.67 ± 0.48	0.63 ± 0.38	42.98 ± 0.11
5	3.254	...	3	0.62	0.79	79.96 ± 10.98	10.28 ± 0.37	2.34 ± 0.27	0.05 ± 0.11	2.66 ± 0.44	1.30 ± 0.35	43.55 ± 0.05
6	3.254	...	3	0.57	0.20	362.89 ± 58.42	9.42 ± 0.42	1.80 ± 0.28	-0.20 ± 0.27	2.27 ± 0.59	1.08 ± 0.48	43.60 ± 0.03
7	3.256	...	2	0.50	-0.01	291.15 ± 71.03	9.17 ± 0.44	1.44 ± 0.26	0.68 ± 0.35	43.10 ± 0.05
8	3.254	...	3	0.53	0.34	138.95 ± 18.62	9.77 ± 0.34	2.03 ± 0.22	-0.36 ± 0.20	2.65 ± 0.44	0.95 ± 0.34	43.39 ± 0.04
9	3.256	...	3	0.42	0.03	196.07 ± 56.84	9.22 ± 0.35	1.26 ± 0.30	-0.67 ± 0.26	1.61 ± 0.32	0.45 ± 0.25	42.93 ± 0.08
10 ^d	3.256	...	2	1.61	0.93	213.02 ± 5.69	11.36 ± 0.16	2.01 ± 0.18	0.79 ± 0.16	44.24 ± 0.01
11	3.256	...	3	0.65	0.36	255.78 ± 78.04	9.29 ± 0.57	1.46 ± 0.23	0.08 ± 0.20	2.23 ± 0.56	1.30 ± 0.45	43.22 ± 0.07
12	3.253	...	2	0.66	0.19	278.28 ± 63.18	9.41 ± 0.52	1.48 ± 0.25	0.89 ± 0.38	43.32 ± 0.05
13	3.254	3.232	2	0.85	0.71	483.14 ± 44.47	10.15 ± 0.54	2.32 ± 0.15	0.19 ± 0.06	3.12 ± 0.42	1.87 ± 0.35	44.17 ± 0.01
14	3.253	3.244	5	0.49	0.23	172.30 ± 53.99	9.40 ± 0.40	1.42 ± 0.34	-0.23 ± 0.28	1.71 ± 0.54	0.74 ± 0.43	43.10 ± 0.09
15	3.253	3.248	4	0.33	0.26	159.33 ± 39.93	9.37 ± 0.42	1.51 ± 0.30	-0.30 ± 0.26	1.42 ± 0.36	0.57 ± 0.28	43.31 ± 0.07
16	3.256	...	3	0.55	0.14	180.40 ± 63.89	9.30 ± 0.44	1.25 ± 0.33	0.64 ± 0.39	42.96 ± 0.10
17	3.262	...	3	0.59	0.28	129.54 ± 38.17	9.50 ± 0.37	1.47 ± 0.31	-0.44 ± 0.29	2.23 ± 0.50	0.76 ± 0.39	43.08 ± 0.09
18	3.254	3.225	4	0.48	-0.01	317.15 ± 96.49	9.16 ± 0.49	1.29 ± 0.28	-0.23 ± 0.28	1.42 ± 0.45	0.66 ± 0.36	43.09 ± 0.07
19	3.254	...	2	0.44	0.25	160.80 ± 63.35	9.37 ± 0.31	1.23 ± 0.24	0.08 ± 0.18	1.15 ± 0.28	0.60 ± 0.22	43.06 ± 0.11
20	3.254	...	1	0.89	0.47	97.56 ± 46.58	9.63 ± 0.36	1.33 ± 0.23	0.87 ± 0.27	43.30 ± 0.16
21	3.254	...	2	0.82	0.50	98.19 ± 17.73	9.98 ± 0.37	1.83 ± 0.22	1.04 ± 0.34	43.37 ± 0.06
22	3.243	3.208	3	0.38	0.04	112.46 ± 38.68	9.57 ± 0.31	1.26 ± 0.27	-0.30 ± 0.41	0.54 ± 0.30	0.23 ± 0.23	42.85 ± 0.11
23	3.254	3.229	5	0.46	0.04	158.91 ± 22.32	9.59 ± 0.36	1.72 ± 0.28	-0.31 ± 0.24	1.52 ± 0.42	0.62 ± 0.33	43.28 ± 0.04
24	3.256	...	2	0.50	0.00	228.56 ± 40.00	9.43 ± 0.41	1.54 ± 0.30	-0.57 ± 0.27	1.75 ± 0.40	0.59 ± 0.32	43.28 ± 0.05
25	3.251	...	3	0.76	0.56	127.21 ± 37.46	9.84 ± 0.39	1.54 ± 0.30	-0.25 ± 0.29	2.87 ± 0.56	1.10 ± 0.46	43.24 ± 0.10
26	3.253	...	2	0.46	0.06	235.85 ± 63.68	9.30 ± 0.39	1.45 ± 0.25	-0.15 ± 0.23	1.47 ± 0.40	0.70 ± 0.32	43.17 ± 0.06
27	3.254	...	2	0.83	0.62	162.22 ± 37.54	9.92 ± 0.47	1.72 ± 0.24	-0.07 ± 0.25	2.80 ± 0.66	1.37 ± 0.54	43.54 ± 0.07
28	3.250	3.217	2	1.00	0.51	264.72 ± 20.56	10.51 ± 0.14	1.21 ± 0.32	-0.24 ± 0.38	0.55 ± 0.36	0.24 ± 0.27	43.34 ± 0.02
29	3.252	...	2	0.64	0.28	108.63 ± 27.47	9.59 ± 0.30	1.67 ± 0.20	0.78 ± 0.23	43.17 ± 0.08
30	3.251	...	3	0.43	0.00	357.10 ± 194.67	8.96 ± 0.42	1.05 ± 0.22	-0.10 ± 0.27	1.18 ± 0.34	0.59 ± 0.27	42.89 ± 0.11
31	3.260	...	3	0.62	0.29	121.42 ± 37.10	9.63 ± 0.44	1.45 ± 0.41	-0.27 ± 0.31	1.86 ± 0.62	0.78 ± 0.50	43.11 ± 0.10
32	3.260	...	2	0.78	0.65	336.53 ± 92.54	9.56 ± 0.45	1.83 ± 0.17	0.14 ± 0.17	3.02 ± 0.53	1.79 ± 0.43	43.79 ± 0.06
33	3.254	...	1	1.09	0.56	74.43 ± 11.17	10.56 ± 0.38	1.93 ± 0.20	0.83 ± 0.22	43.58 ± 0.05
34	3.251	...	5	0.31	0.47	91.94 ± 18.67	9.16 ± 0.42	1.25 ± 0.15	-0.03 ± 0.23	1.93 ± 0.58	0.96 ± 0.47	42.67 ± 0.04

Notes.^a Morphology Type: 1—UV faint; 2—compact; 3—diffuse/clumpy/tidal; 4—merger; 5—multiple components.^b A typical error of $U - V$ is 0.12.^c A typical error of $V - J$ is 0.24.^d X-ray source (with XID = 760 in the Chandra 7 Ms catalog).

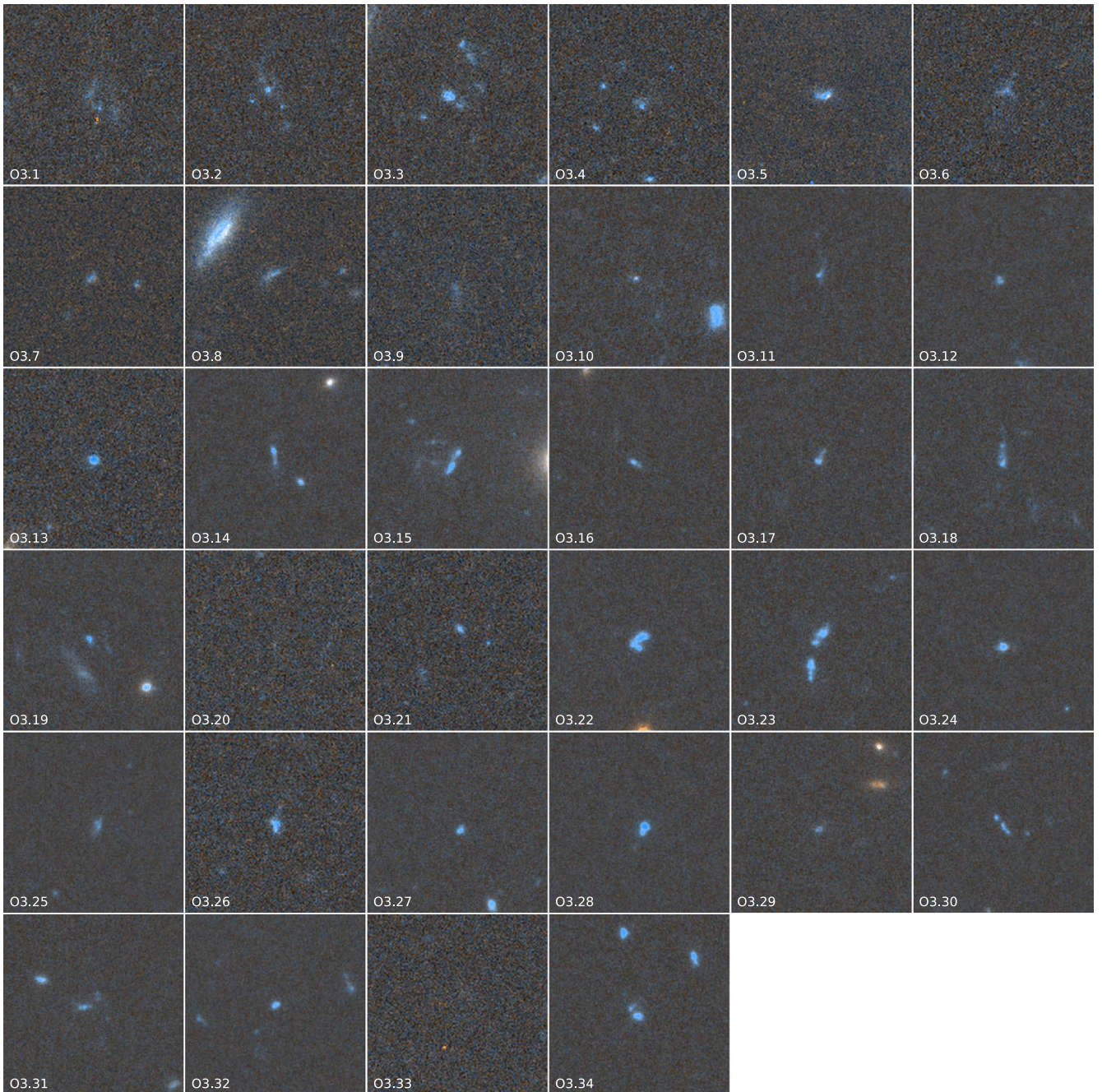


Figure 3. HST/ACS stamp images for our sample of 34 [O III] ELGs. Each stamp is given in a size of $6'' \times 6''$, corresponding to $45 \text{ kpc} \times 45 \text{ kpc}$ at $z \sim 3.25$. These color images are made with HST/ACS V_{606} and z_{850} images from the GEMS and CANDELS surveys. Note that three images (ID = 6, 7, 8) are made with I_{814} and z_{850} images owing to the lack of V_{606} observations.

Our results of morphological classifications show that about 6% (2/34) are too faint to be securely resolved in both V_{606} and z_{850} ; 35% (12/34) appear to be compact with $R_e < 0''.3$, and the majority of these compact ones are relatively bright; 38% (13/34) of our sample [O III] ELGs have diffuse emission out to $R = 1'' - 2''$ (7–15 kpc) or have apparent tidal/clumpy features within $1''$; 9% (3/34) look like mergers, with two obvious galactic nuclei connected by tidal bridges; and 12% (4/34) are pairs of two or three components with comparable colors and sizes and are separated by $< 2''$ without clear tidal bridges between them.

There are 20 sample ELGs having the HST/WFC3 J_{125} and H_{160} images from CANDELS. For $z \sim 3.25$, these two bands

correspond to the rest-frame NUV (2939 Å) and U (3624 Å). Figure 4 presents their color images made with the two-band data. We carry out morphological classification with the J_{125} and H_{160} images. The results are very similar to those based on the $V_{606} + z_{850}$ images. Note that one object (ID = 20) is invisible in V_{606} and z_{850} and appears as a compact galaxy in J_{125} and H_{160} . We take the morphological classifications based on V_{606} and z_{850} as our main morphology properties for these 34 [O III] ELGs.

We point out that there are two UV-faint [O III] ELGs (ID = 20, 33) being heavily attenuated by dust in rest-frame UV. As shown in Figure 2, these two objects' SEDs show clear dust reddening, while several other objects (e.g., ID = 10, 12,

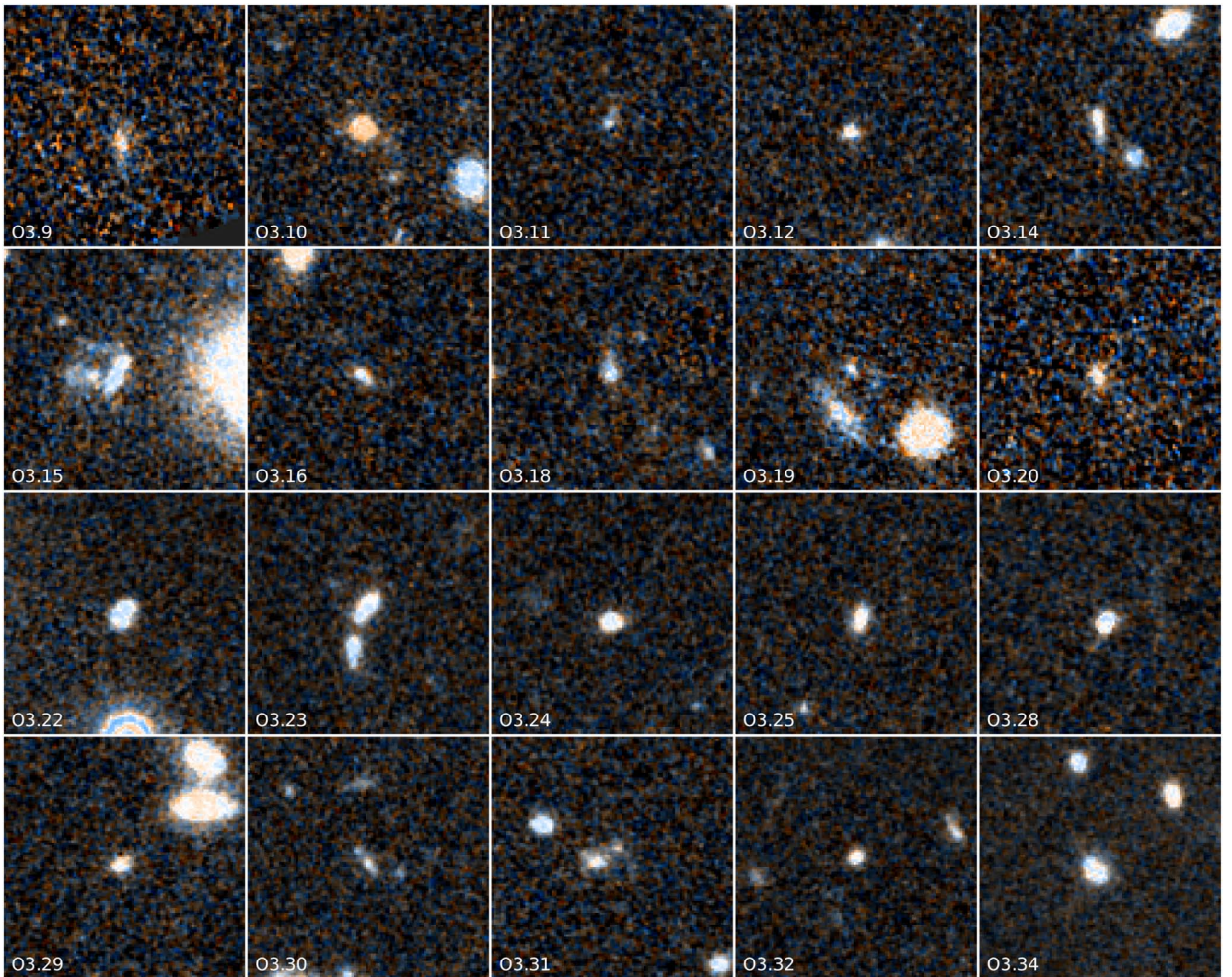


Figure 4. HST/WFC3 stamp images of 20 [O III] ELGs in our sample. The color images are made with HST/WFC3 J_{125} and H_{160} images from CANDELS (the same size as given in Figure 3).

29) also exhibit reddening from their SEDs. We find that these galaxies are all compact, indicating that the compactness helps to maintain a dustier star-forming environment, although the rest-UV morphologies are very sensitive to young stellar populations with large uncertainties due to dust attenuation. We stress that our sample selection based on the $H_2S(1)$ and K_s observations is able to pick these dusty [O III] ELGs, which were missed by the previous studies based on the optical sample selections.

4.3. Colors and [O III] EWs

The UVJ diagram is widely used to separate SFGs and quiescent galaxies (Williams et al. 2009; Brammer et al. 2011; Whitaker et al. 2011). Similarly, the U and V filters given in Maíz Apellániz (2006) and the J filter from the Two Micron All Sky Survey (2MASS) are adopted to derive the rest-frame $U - V$ and $V - J$ colors from the best-fit model SEDs of our [O III] ELGs. The calculation is done with CIGALE (Boquien et al. 2019). Figure 5 shows the distribution of our [O III] ELGs in the rest-frame $U - V$ and $V - J$ diagrams. The stellar masses derived from CIGALE are used to color-code the data points. The selection criteria to distinguish star-forming and quiescent

galaxies are adopted from Williams et al. (2009). For a comparison, we also show a sample of galaxies with $9 < \log(M_*/M_\odot) < 11$ at $2.8 < z < 3.7$ from the 3D-HST GOODS-South catalog (Skelton et al. 2014).

It is clear from Figure 5 that all of our sample [O III] ELGs are located in the star-forming regime, except for the AGN host with $U - V = 1.6$ owing to strong dust attenuation. This confirms that the vast majority of our [O III] sample galaxies are SFGs. About 56% (19/34) of the [O III] ELGs with $V - J < 0.3$ are very blue, likely being little affected by dust attenuation or boosted in V by strong [O III] emission. Meanwhile, the [O III] ELGs of lower stellar masses tend to have bluer colors in both $U - V$ and $V - J$, consistent with the results for the overall galaxy population (Skelton et al. 2014; Straatman et al. 2016).

As described in Section 2.1 (see also A14), the rest-frame EWs of our [O III] samples are estimated using the formula from Geach et al. (2008) as

$$EW_{[\text{O III}]} = \frac{\Delta\lambda_{H_2S(1)} \times (f_{H_2S(1)} - f_{K_s})}{[f_{K_s} - f_{H_2S(1)} (\Delta\lambda_{H_2S(1)} / \Delta\lambda_{K_s})] \times (1 + z)}, \quad (2)$$

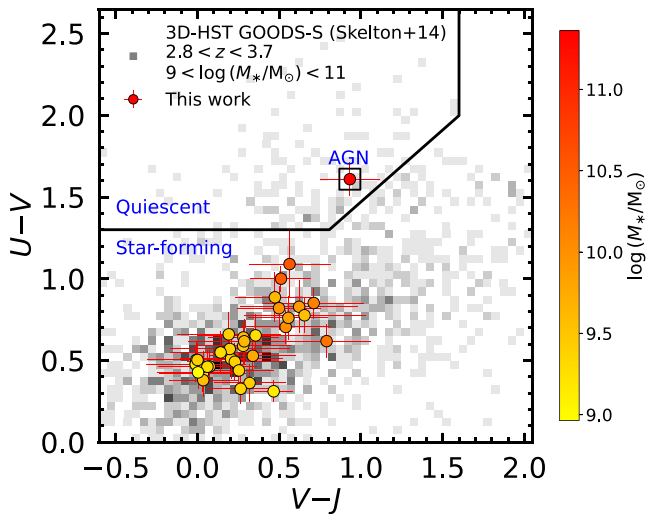


Figure 5. Rest-frame UVJ color diagram of 34 [O III] ELGs color-coded with stellar mass. The gray density map shows the distribution of galaxies selected with $9 < \log(M_*/M_\odot) < 11$ at $2.8 < z < 3.7$ from the 3D-HST GOODS-South catalog. The selection box to separate star-forming and quiescent galaxies is from Williams et al. (2009). The AGN source in the regime of quiescent galaxies is marked with a black square. Our sample [O III] ELGs are mostly located at the blue end of the star-forming regime.

where $\Delta\lambda_{H\beta S(1)}$ and $\Delta\lambda_{K_s}$ are the widths of the narrow- and broadband filters and $f_{H\beta S(1)}$ and f_{K_s} are the flux densities in these two bands. The estimated EWs are listed in Table 3.

The [O III] EWs of our sample ELGs vary over a wide range from 70 to 500 Å, with a median value of ~ 200 Å, and 15% of them are larger than 300 Å. The relation between A_V derived from CIGALE fitting and EW is shown in Figure 6. There are eight sample galaxies having $A_V > 1$ mag, showing a relatively high fraction of dusty [O III] ELGs. The majority of the [O III] ELGs with $A_V < 1$ mag have [O III] EWs over 70–400 Å. Further discussion about the rest-frame EWs of our [O III] ELGs will be presented in Section 6.2.

4.4. Stellar Mass and SFR

Galaxy properties estimated through SED fitting with CIGALE are listed in Table 3. The stellar mass versus SFR relation of our [O III] ELG sample is shown in Figure 7. For a comparison, we also include other samples of [O III] ELGs at similar redshifts from the literature, including [O III] emitters at $z \sim 3.2$ from Suzuki et al. (2015) and at $z \sim 3.3$ from Onodera et al. (2016, 2020).

We perform an orthogonal distance regression (ODR) fit to the data points of our sample and estimate the dispersion. For our 33 [O III] SFGs, the ODR fit gives a best-fit slope of 0.67 and a median dispersion of 0.15 dex, while the other three works hold a dispersion of 0.16, 0.23, and 0.16 dex for Suzuki et al. (2015), Onodera et al. (2016), and Onodera et al. (2020), respectively. The solid gray curve shows the best-fit relation for the star-forming main sequence (SFMS) of SFGs at $z \sim 3.25$ given in Tomczak et al. (2016), and the shaded area represents a dispersion of 0.3 dex. The gray dashed line denotes the timescale of 100 Myr for a galaxy doubling stellar mass, and the majority of our [O III] sample SFGs are located around this line and mostly above the MS. It is clear that the majority of our [O III] ELGs have relatively higher SFRs than typical SFGs of the same masses at similar redshifts. The dispersion of our

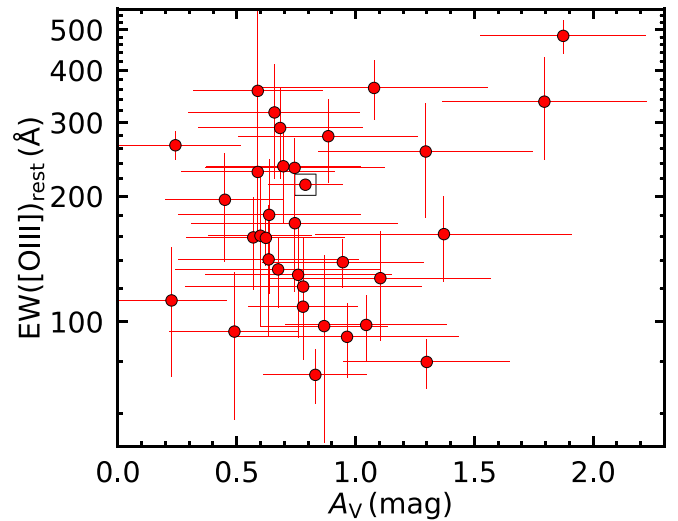


Figure 6. A_V vs. rest-frame [O III] EW for our sample of [O III] ELGs. The majority of our sample galaxies have rest-frame [O III] EWs in 100–300 Å with a median EW of 194 Å, suggestive of the presence of strong [O III] emission line. For those with $A_V < 1$ mag, the [O III] EW varies from 70 to 400 Å.

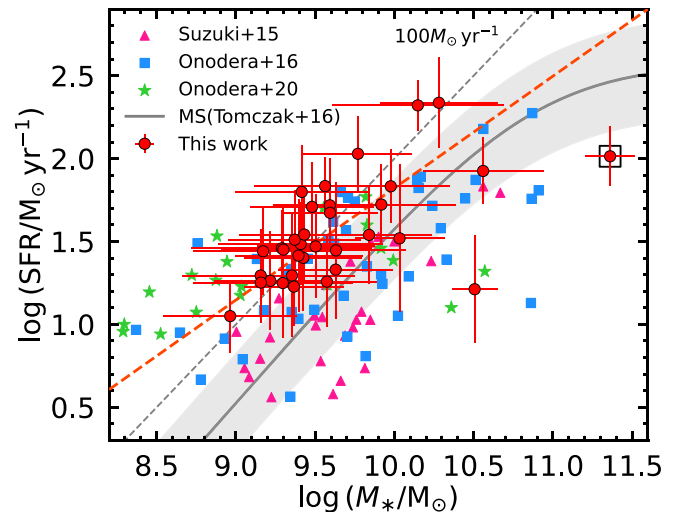


Figure 7. Relationship between stellar mass and SFR for our 34 [O III] ELGs at $z \sim 3.25$ (red circles), in comparison with [O III] ELGs at $z \sim 3.2$ from Suzuki et al. (2015; pink triangles), at $z \sim 3.3$ from Onodera et al. (2016; blue squares), and at $z \sim 3.3$ from Onodera et al. (2020; green stars). The red dashed line is the best fit to our 33 [O III] ELGs (excluding the X-ray source), giving a best-fit slope of 0.69. The gray solid curve represents the best fit for the SFMS of SFGs at $z \sim 3.25$ given in Tomczak et al. (2016), with the shaded area showing a 0.3 dex dispersion. The gray dashed line shows the timescale of 100 Myr for a galaxy doubling stellar mass. Most of our sample [O III] ELGs lie above the SFMS with higher SFRs.

sample galaxies is comparable to that of other [O III] ELG samples.

In addition, compact SFGs tend to be found at the upper envelope of the SFMS (e.g., Barro et al. 2017; Gómez-Guijarro et al. 2019). Our [O III] ELGs are mainly young and blue SFGs with strong star formation activities, and more than one-third of our sample galaxies are classified as compact ones in terms of their morphologies in the rest-frame UV. We thus argue that the compact [O III] ELGs in our sample resemble compact SFGs at $z \sim 3.25$ as young starburst galaxies with high SFRs.

4.5. Dust Attenuation

The empirical dust attenuation curve of Calzetti et al. (2000) is widely used for starburst galaxies. Noll et al. (2009) modified the Calzetti law by multiplying a power-law function with a slope of δ and adding a 2175 Å bump that is described by a Lorentzian-like Drude profile. We take the modified Calzetti law as the dust attenuation curve in our analysis and derive dust attenuation A_V from the SED fitting with CIGALE. In practice, the stellar color excess $E(B-V)_{\text{star}}$ and attenuation curve slope δ are set as free parameters in the fitting.

From the best-fit results with CIGALE, we obtain $E(B-V)_{\text{star}}$, δ , and the strength of the 2175 Å bump for each sample galaxy. We are able to estimate the attenuation at a given band using the global attenuation formula from Boquien et al. (2019) as

$$k_\lambda = (k_\lambda^{\text{starburst}} \times (\lambda/550 \text{ nm})^\delta + D_\lambda) \times \frac{E(B-V)_{\delta=0}}{E(B-V)_\delta}, \quad (3)$$

where D_λ is the Drude profile that describes the 2175 Å bump, and the last term renormalizes the curve so that $E(B-V)$ remains equal to the input $E(B-V)$ when $\delta \neq 0$. We then estimate the attenuation to the [O III] $\lambda 5007$ line A_{OIII} with this equation, and the results are shown in Table 3.

It can be clearly seen from Figure 2 that the 2175 Å bump is present in the best-fit SEDs of seven sample galaxies (e.g., ID = 5 and 13). The 2175 Å bump is redshifted to around 9250 Å at $z \sim 3.25$, corresponding to I and z_{850} . These seven galaxies have relatively high SFRs and A_{OIII} . Moreover, half of them are compact, and the other half are extended in morphology. We do not see a connection between the presence of the 2175 Å bump and galaxy morphology among these $z \sim 3.25$ [O III] ELGs.

Previous studies reported that the 2175 Å bump is commonly seen in SFGs up to $z \sim 2.6$ (Buat et al. 2011; Wild et al. 2011; Shivaei et al. 2020; Kashino et al. 2021). Noll et al. (2009) pointed out that at least 30% of SFGs at $1 < z < 2.5$ exhibit a significant 2175 Å bump. In our SED fitting, the 2175 Å bump is introduced when the z_{850} flux is lower than the I flux in an SED. We caution that either an overestimate of the I flux or an underestimate of the z_{850} flux might demand a stronger 2175 Å bump in the models for a better fit. We examine the 2175 Å bump of those best-fit SEDs, finding that most of the seven sample galaxies have a higher I flux than the z_{850} . Due to the lack of spectroscopic and more photometric data, it is difficult to securely confirm the 2175 Å bump. More efforts are necessary to investigate the origin of the 2175 Å bump in $z \sim 3.25$ [O III] ELGs.

We estimate A_{FUV} at 1500 Å with Equation (3) and show the correlation between A_{FUV} and UV slope β in Figure 8. There are eight sample galaxies that are compact ($R < 0''.1$), faint, or nearly invisible in the rest-frame UV (see Figure 3), indicating a highly obscured environment around these galaxies. In addition, these sources also show upper limits in both U and B in their SEDs (see Figure 2); therefore, the UV slope β becomes meaningless for such a case. Thus, these eight sources are not included in Figure 8. The UV slope β is often used as a measure of dust obscuration in the sense that a redder UV slope (a higher β) is linked to a higher dust attenuation (Meurer et al. 1999). From Figure 8, however, we show that our sample galaxies do not exhibit a clear correlation between β and A_{FUV} . As can be seen, some of our sample galaxies are barely visible

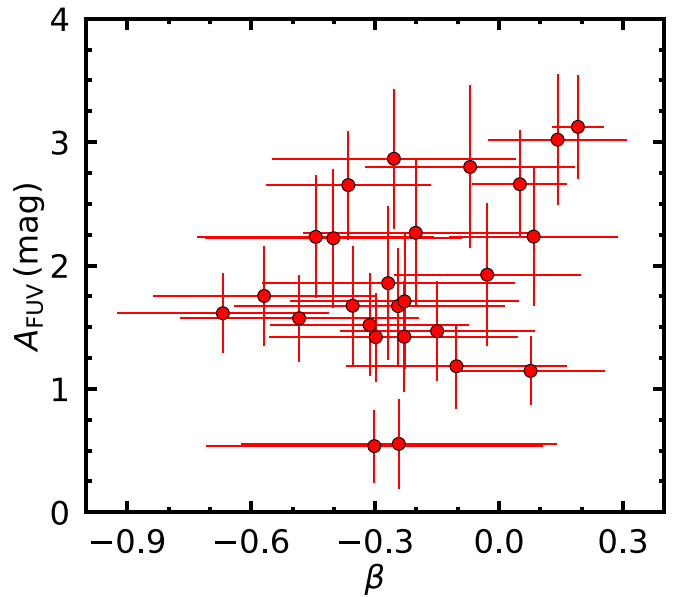


Figure 8. UV slope β vs. dust attenuation in the FUV A_{FUV} for our sample of 26 [O III] ELGs. Eight faint sources with upper limits in both U and B are ignored since the measurements of their A_{FUV} and β are largely uncertain. The scatter is large owing to the lack of UV photometric data.

in the rest-frame FUV owing to the heavy dust attenuation, and the estimates of β and A_{FUV} could be significantly biased by the leaking UV radiation.

4.6. [O III] Luminosity

Following Ly et al. (2011), we estimate the line flux of [O III] $\lambda 5007$ from the narrowband excess using

$$F_{[\text{OIII}]} = \Delta\text{NB} \frac{f_{\text{NB}} - f_{K_s}}{1 - (\Delta\text{NB}/\Delta K_s)}, \quad (4)$$

where $F_{[\text{OIII}]}$ is the integrated line flux of [O III] given in units of $\text{erg s}^{-1} \text{cm}^{-2}$, and f_{NB} and f_{K_s} refer to fluxes in $\text{H}_2\text{S}(1)$ and K_s , respectively, given in the units of $\text{erg s}^{-1} \text{cm}^{-2} \text{\AA}^{-1}$. The bandwidths are $\Delta\text{NB} = 293 \text{ \AA}$ and $\Delta K_s = 3250 \text{ \AA}$. We note that our sample was selected with $\text{EW} > 50 \text{ \AA}$ and the 5σ detection limits are $\text{H}_2\text{S}(1) = 22.8 \text{ mag}$ and $K_s = 24.8 \text{ mag}$. The detection limit for the [O III] emission line is then estimated to be $> 2.5 \times 10^{-17} \text{ erg s}^{-1} \text{cm}^{-2}$. These luminosities are corrected for dust attenuation with A_{OIII} . We calculate the [O III] line luminosity for our sample galaxies and present them in Table 3.

Figure 9 shows the relation between SFR and [O III] luminosity. A strong correlation is seen. Such a correlation has been reported before (e.g., Straughn et al. 2009; Villavélez et al. 2021). It is also clear that most of our [O III] ELGs have dust-corrected luminosities in the range of $10^{42.6} - 10^{43.6}$. In order to show the representativeness of luminosity for our [O III] ELGs, the luminosity functions of [O III] ELGs at $z \sim 3.24$ from Khostovan et al. (2015) are adopted for comparison. Note that the luminosity function parameter results in their work are uncorrected for dust and AGN contribution owing to the undeveloped roles of dust on emission lines at the high- z universe. The characteristic luminosity of [O III] ELGs at $z \sim 3.24$ in Khostovan et al. (2015) is $\log L_* = 42.83 \text{ erg s}^{-1}$, while the median value of the

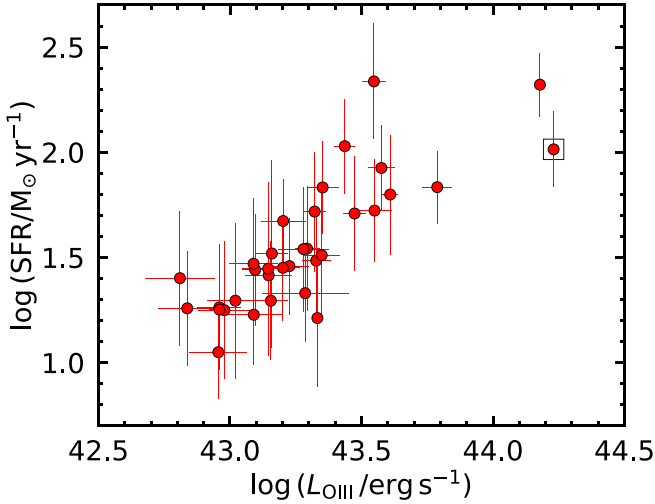


Figure 9. Relationship between [O III] luminosity and SFR. The [O III] luminosities are corrected for dust attenuation obtained from CIGALE. It is clear that SFR increases with [O III] luminosity in a statistic manner.

uncorrected luminosity of our [O III] sample is $10^{42.73} \text{ erg s}^{-1}$, showing a variance of 0.1 dex. The similarity in uncorrected [O III] luminosity indicates that our [O III] sample shows a typical property of luminosity at this redshift.

5. An Overdensity Traced by [O III] ELGs

Figure 10 shows the spatial distribution of our sample of 34 [O III] ELGs. It is obvious that they are strongly clustered and form an overdensity. We estimate its overdensity factor as $\delta_{\text{gal}} = N_{\text{group}}/N_{\text{field}} - 1$. The effective detection area of our sample is 383 arcmin^2 . The narrowband filter H₂S(1) ($\lambda_c = 2.130 \mu\text{m}$, $\Delta\lambda = 0.0293 \mu\text{m}$) covers a redshift span of $z = 3.254 \pm 0.029$ for [O III] $\lambda 5007$, corresponding to a radial scale of 50.9 comoving Mpc (cMpc). The total comoving volume of ECDFS is then estimated to be 41.5^3 cMpc^3 .

5.1. General Field Number Density

In order to estimate the overdensity factor of [O III] ELGs in ECDFS, we first estimate the number density in general fields. The High-redshift(Z) Emission Line Survey (HiZELS) provides a large sample of ELGs identified by narrowband excesses in COSMOS and UDS (Sobral et al. 2013). The NB_K filter ($\lambda_c = 2.1210 \mu\text{m}$, $\Delta\lambda = 0.0210 \mu\text{m}$) probes [O III] ELGs at $z \sim 3.24$, which is similar to our sample galaxies. Given that the improved photometric catalog is available in COSMOS, we cross the NB_K-excess object catalog from Sobral et al. (2013) with the COSMOS2020 catalog (Weaver et al. 2022) to identify the [O III] ELGs in COSMOS. Following the selection criteria used in Khostovan et al. (2015), we pick in total 159 NB_K-excess objects with $2.8 \leq z_{\text{phot}} \leq 4$ to be [O III] ELGs. We use this sample to estimate the number density of [O III] ELGs at $z \sim 3.24$ in general fields.

The selection criterion for ELGs ($\text{EW} > 25 \text{ \AA}$) from Sobral et al. (2013) differs from ours ($\text{EW} > 50 \text{ \AA}$). And the detection limits on narrow- and broadband depths also affect the selection for [O III] emitters. We apply our [O III] ELG selection criteria ($\text{EW} > 50 \text{ \AA}$, $\text{H}_2\text{S}(1) < 22.8 \text{ mag}$, and $K_s < 24.8 \text{ mag}$) to the selected 159 [O III] emitters in COSMOS, given that 157 of the 159 [O III] emitters meet our selection criteria. [O III] ELGs at this redshift usually have a high EW; therefore, the difference

between two EW cuts has a negligible impact on the selection. The effective sky coverage for these [O III] ELGs is $\sim 1.6 \text{ deg}^2$, while the NB_K filter covers a comoving distance in the line of sight with 37.1 cMpc. So the total volume of these 157 [O III] emitters is about $7.8 \times 10^5 \text{ cMpc}^3$. We estimate the number density per volume of [O III] ELGs in COSMOS to be $2.0 \times 10^{-4} \text{ cMpc}^{-3}$. Khostovan et al. (2015) showed an H β + [O III] number density of $2.3 \times 10^{-4} \text{ cMpc}^{-3}$ at $2.8 \leq z_{\text{phot}} \leq 4$ in COSMOS and UDS, while Forrest et al. (2017) presented the strong [O III] ELG number density of $2.3 \times 10^{-4} \text{ cMpc}^{-3}$ at $2.5 \leq z_{\text{phot}} \leq 4$ in CDFS. This indicates that our number densities are comparable to other studies. So we take this to be the number density of $z = 3.25$ [O III] ELGs in general fields.

5.2. Density Map and δ_{gal}

Our sample includes 34 [O III] ELGs detected over 383 arcmin^2 in ECDFS and a redshift span of $z = 3.254 \pm 0.029$, giving a number density of [O III] ELGs $(4.8 \pm 0.8) \times 10^{-4} \text{ cMpc}^{-3}$. We note that our sample [O III] ELGs are located in a smaller area than the detection area. We construct a density map for our $z \sim 3.25$ [O III] ELGs and estimate the coverage area of the overdensity in ECDFS. Following Zheng et al. (2021), the detection area is divided into a grid of $1' \times 1'$ cells, and the number of ELGs is counted in each cell to obtain the number density. A Gaussian kernel of $\sigma = 1'$ (i.e., 1.9 cMpc at $z \sim 3.25$) is used to convolve the grid and yield the density map as shown in Figure 10. The contour levels are drawn at 4, 8, 12, 16, and 20 \times the surface [O III] emitter number density of general fields.

Clearly, the majority of our sample galaxies are located in the central region of ECDFS. The red solid rectangle in Figure 10 encloses 31 [O III] ELGs over an area of 170.7 arcmin^2 ($17'.5 \times 9'.7$). The density map of [O III] ELGs consists of two components: one southeast (SE) composed of 15 [O III] ELGs over 35.0 arcmin^2 ($7' \times 5'$), and the other northwest (NW) with seven sample galaxies over 19.4 arcmin^2 ($4'.4 \times 4'.4$). Four spectroscopically identified [O III] ELGs are also located in the SE component, confirming that this overdensity region is located at $z \sim 3.25$.

We then estimate the volume number density of [O III] ELGs in these components. We note that the redshift span of $z = 3.254 \pm 0.029$ used to calculate the radial scale may be too large for calculating the comoving volumes because our sample [O III] ELGs unlikely fulfill the bandwidth of H₂S(1) and the actual radial size of the [O III] overdensity is smaller than 50.9 cMpc. Given that the available spec- z of our sample [O III] ELGs are all at $z < 3.255$, the half of the redshift span covered by the H₂S(1) filter (see Figure 1), we thus take half of the radial comoving distance (25.5 cMpc) to be the upper limit for the radial size of the [O III] overdensity. On the other hand, the radial size of the overdensity is unlikely smaller than the minor axis of each component area, giving a lower limit of the radial comoving distance. Therefore, we take the lower and upper limits of the radial size to estimate the comoving volume for these three components.

The red solid rectangle area covers a comoving volume from 25^3 to 23^3 cMpc^3 . We then estimate the [O III] overdensity to have a volume number density from $(1.9 \pm 0.4) \times 10^{-3} \text{ cMpc}^{-3}$ to $(2.7 \pm 0.5) \times 10^{-3} \text{ cMpc}^{-3}$, giving δ_{gal} in the range of $[8.7 \pm 2.0, 12.3 \pm 2.8]$. The SE component contains 15 objects in a comoving volume from 15^3 to 11^3 cMpc^3 , giving a volume number density from $(4.6 \pm 1.2) \times 10^{-3} \text{ cMpc}^{-3}$ to $(12.1 \pm 3.2) \times 10^{-3} \text{ cMpc}^{-3}$ and δ_{gal} in the range of $[21.8 \pm 5.7, 59.5 \pm 16.9]$.

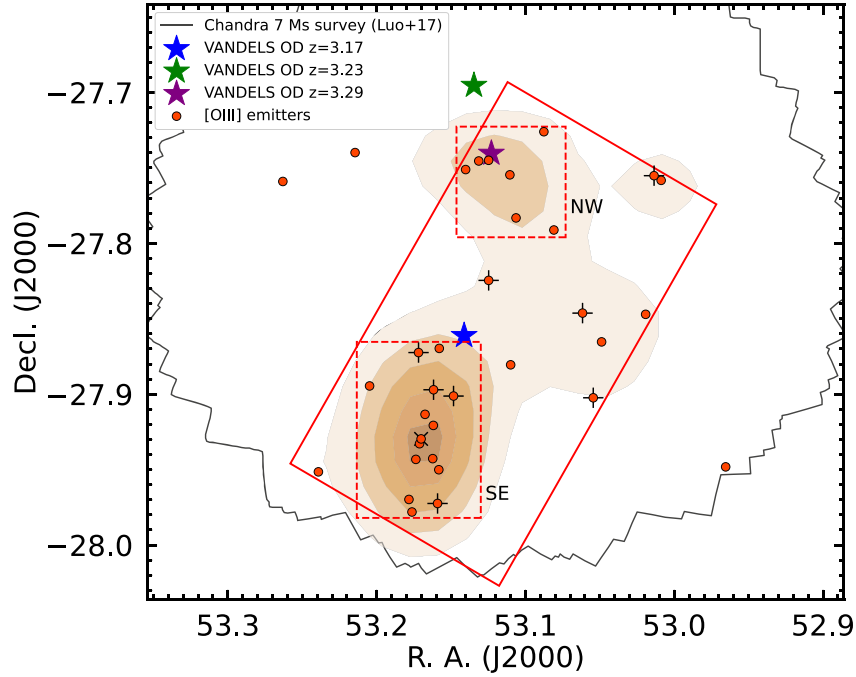


Figure 10. Spatial distribution of 34 [O III] ELGs at $z \sim 3.25$ in ECDFS. Red circles represent our [O III] ELGs, and plus signs denote the spectroscopically confirmed ones. The cross marks the AGN source. The contour levels of the density map refer to $[4, 8, 12, 16, 20] \times$ the [O III] emitter surface number density of general fields ($2.7 \times 10^{-2} \text{ arcmin}^{-2}$). The red solid rectangle covers 31 sources with an area of $17'.5 \times 9'.7$. The southeast (SE) component ($7' \times 5'$) and the northwest (NW) component ($4'.4 \times 4'.4$) cover 15 and 7 sources, respectively. The stars mark the locations of identified overdensities traced by Ly α emitters at similar redshifts in CDFS from the VANDALS survey (Guaita et al. 2020). Black solid lines show the coverage of Chandra 7 Ms X-ray observations.

The NW component contains seven objects in the volume from 12^3 to 8^3 cMpc^3 , yielding a number density of $(3.9 \pm 1.7) \times 10^{-3} \text{ cMpc}^{-3}$ to $(11.7 \pm 5.0) \times 10^{-3} \text{ cMpc}^{-3}$. And the δ_{gal} of NW varies in the range of $[18.2 \pm 8.4, 57.1 \pm 25.4]$. The uncertainties are simply estimated by shot noise. These estimated overdensity factors confirm that our sample [O III] ELGs in ECDFS reside in an overdensity.

5.3. Present-day Mass

The typical size of a protocluster at $z = 3$ is about 20 cMpc (Chiang et al. 2013). We estimate the expected total mass at $z \sim 0$ for the overdensity components at $z = 3.25$ in ECDFS using

$$M_{z=0} = \bar{\rho}(1 + \delta_m)V_{\text{true}}, \quad (5)$$

from Steidel et al. (1998). Here $\bar{\rho}$ is the mean comoving matter density of the universe, which equals $\frac{3H_0^2}{8\pi G} = 4.1 \times 10^{10} M_{\odot} \text{ cMpc}^{-3}$; δ_m is the matter overdensity; and $V_{\text{true}} = V_{\text{obs}}/C$. From Steidel et al. (1998), V_{obs} is the observed comoving volume and C is a correction factor estimated using $C = 1 + f - f(1 + \delta_m)^{1/3}$, where $f = \Omega_m z^{4/7}$ and $f = 0.98$ at $z = 3.25$. And δ_m is linked to the galaxy overdensity by $1 + b\delta_m = C(1 + \delta_{\text{gal}})$, where b is the [O III] emitter bias factor. We adopt the linear bias $b = 3.43$ for [O III] ELGs in the redshift range of 2–3 from Zhai et al. (2021) as the bias for [O III] ELGs at $z = 3.25$.

We calculate the correction factor C and matter overdensity δ_m for two overdensity components. For the SE substructure, we obtain $\delta_m = 4.33$ and $C = 0.27$ for the lower limits and $\delta_m = 2.67$ and $C = 0.47$ for the upper limits. For the NW substructure, we obtain $\delta_m = 4.26$ and $C = 0.27$ for the lower

limits and $\delta_m = 2.39$ and $C = 0.51$ for the upper limits. And for the entire structure, we get $\delta_m = 1.83, 1.40$ and $C = 0.59, 0.67$ for the lower and upper limits, respectively. So the present-day mass is then estimated to be $\sim 1.1 \times 10^{15} M_{\odot}$ for the SE substructure and $\sim 4.8 \times 10^{14} M_{\odot}$ for the NW substructure. And the present-day mass of the entire structure is $\sim 2.3 \times 10^{15} M_{\odot}$.

Based on these estimates, we conclude that the overdensity traced by our [O III] ELGs is indeed a massive protocluster of galaxies at $z \sim 3.25$ in ECDFS. These two substructures are expected to become virialized at $z = 0$, with the SE substructure probably being a high-mass ‘‘Coma-type’’ cluster of $\sim 10^{15} M_{\odot}$ and the NW substructure forming an intermediate-mass ‘‘Virgo-type’’ cluster of $(3\text{--}9) \times 10^{14} M_{\odot}$. Moreover, the two substructures are separated by 21.8 cMpc, which is the characteristic size of a massive protocluster at $z \sim 3$, and they probably merge into a more massive Coma-like galaxy cluster in the present day.

6. Discussion

6.1. Contribution of H β and [O III] $\lambda 4959$ Emission Lines

We take [O III] $\lambda 5007$ at $z \sim 3.25$ as the emission line detected by the flux excess in the narrowband H $_2$ S(1). Given that H β and [O III] $\lambda 4959$ are close to [O III] $\lambda 5007$, it is possible that H β and [O III] $\lambda 4959$ might contaminate our sample selection.

We notice that the bandwidth of H $_2$ S(1) is too narrow to cover both H β and [O III] lines simultaneously. Khostovan et al. (2015) pointed out that the [O III] line dominates the population in H β + [O III] luminosity function, with the fraction of H β emitters decreasing at the increasing H β + [O III] line luminosity. Similarly, Suzuki et al. (2016) examined the contamination to [O III] $\lambda 5007$ at $z = 2.23$ and found that the

contribution of $H\beta$ is only $\sim 3\%$, while [O III] $\lambda 4959$'s contribution is up to 25%. Our sample [O III] ELGs have bright line luminosities at ~ 3.25 . We argue that the $H\beta$ contribution is negligible in our sample.

The doublet [O III] $\lambda\lambda 4959, 5007$ are separated by $\Delta\lambda = 204 \text{ \AA}$ when they shift to $z \sim 3.25$, and enter the central wavelength of $H_2S(1)$. The two lines can both be covered by the $H_2S(1)$ filter ($\Delta\lambda = 293 \text{ \AA}$) for [O III] emitters at $3.266 < z < 3.283$, compared to the redshift span of $3.225 < z < 3.283$ for [O III] $\lambda 5007$ alone. Therefore, our measurements of the line fluxes of [O III] $\lambda 5007$ could be overestimated by 25% owing to the contribution of [O III] $\lambda 4959$ if our [O III] ELGs are in the redshift range of $3.266 < z < 3.283$. Here a flux ratio of 3 is adopted between [O III] $\lambda 5007$ and [O III] $\lambda 4959$ (Suzuki et al. 2016). We note that seven targets in our sample have spectroscopic redshifts in the range of $3.20 < z < 3.25$ and are spatially mixed with other sample galaxies, implying that our sample galaxies are most likely distributed at $3.225 < z < 3.25$ and the contribution by [O III] $\lambda 4959$ should be ignorable. We thus argue that the [O III] $\lambda 5007$ emission line dominates our sample galaxies.

6.2. Evolution of Extreme [O III] ELGs over $z \sim 3 - 4$

The vast majority of $z > 3$ galaxies are star-forming, and those with strong emission lines are very common at high redshifts. Our sample [O III] ELGs at $z \sim 3.25$ are about 1–2 Gyr before the cosmic star formation peak and are expected to provide clues for understanding how galaxies grow and enhance star formation. The strong [O III] emission lines can be generated from the ionized regions around the hot young massive stars in a galaxy. Galaxies with extremely strong [O III] emission lines at this epoch are found to have preferentially lower metallicity and higher ionization parameters powered by intense star formation activities (Nakajima & Ouchi 2014). The most intense [O III] ELGs are defined as extreme ELGs (EELGs) with a composite rest-frame $EW([\text{O III}])$ of $803 \pm 228 \text{ \AA}$, while the less intense but still significant [O III] ELGs are named strong ELGs (SELGs) with a composite $EW([\text{O III}])$ of $230 \pm 90 \text{ \AA}$ (Forrest et al. 2017).

The [O III] EELGs at $z \sim 3-4$, i.e., those with $EW([\text{O III}]_{\text{rest}}) > 500 \text{ \AA}$, are widely studied in the literature (Forrest et al. 2017; Cohn et al. 2018; Forrest et al. 2018; Onodera et al. 2020; Tran et al. 2020; Tang et al. 2021a, 2021b). They are typically small with $M_* \sim 10^8 - 10^9 M_\odot$ and $SFR \sim 20 - 50 M_\odot \text{ yr}^{-1}$ (Maseda et al. 2014; Tran et al. 2020). At increasing stellar mass, EELGs tend to have higher metallicity and stronger continuum emission from evolved stellar populations. Tran et al. (2020) demonstrated that for EELGs with higher stellar masses, their [O III] $\lambda 5007$ EWs tend to decrease with relatively higher stellar continua at given star formation activities.

Our sample [O III] ELGs are SELGs with a median $EW \sim 200 \text{ \AA}$ in the range of $70 \text{ \AA} < EW([\text{O III}]_{\text{rest}}) < 500 \text{ \AA}$. Our results support the scenario that strong [O III] $\lambda 5007$ emission reveals the early episode of intense star formation. Our sample galaxies have stellar masses larger than $\log(M_*/M_\odot) \sim 9$ and larger SFRs of $10 - 100 M_\odot \text{ yr}^{-1}$, denoting that our [O III] ELGs are more representative of the main population of SFGs than the [O III] EELGs with $EW([\text{O III}]_{\text{rest}}) > 500 \text{ \AA}$.

6.3. The [O III] Overdensity in ECDFS

Protoclusters are considered as ideal laboratories to study galaxy properties in the dense environments, as well as the environmental effects on galaxy formation and evolution. Previous studies on $z > 3$ protoclusters mainly identify them with $\text{Ly}\alpha$ emitters (LAEs), Lyman break galaxies (LBGs), and submillimeter galaxies (SMGs). Up to date, there are more than 30 protoclusters reported at $z > 3$ with spectroscopically confirmed galaxies (see Harikane et al. 2019, for a review). These protoclusters are likely to form ‘‘Virgo-type’’ galaxy clusters at $z = 0$ with a total mass of $(3-9) \times 10^{14} M_\odot$.

Only a few overdensity structures have been reported at $z > 3$ traced with [O III] emitters (Maschietto et al. 2008; Forrest et al. 2017). We show that our sample [O III] ELGs reside in a massive overdense structure in ECDFS. The SE substructure spreads over an area of $7' \times 5'$, while the NW substructure covers an area of $4.4' \times 4.4'$. This overdensity of [O III] ELGs at $z \sim 3.25$ is a new structure discovered in ECDFS. The SE and NW components have an overdensity factor of about 20–60 over different comoving volumes owing to the limits of radial comoving distance. These two substructures are expected to be virialized at $z = 0$ and probably form a massive cluster with $\sim 1.1 \times 10^{15} M_\odot$ for SE and $\sim 4.8 \times 10^{14} M_\odot$ for NW. And the two substructures probably merge into a more massive single Coma-like galaxy cluster with $\sim 2.3 \times 10^{15} M_\odot$.

In ECDFS, there is one overdensity traced by extreme $H\beta + [\text{O III}]$ emitters at $z \sim 3.5$ discovered by the ZFOURGE and GOODS-ALMA surveys (Forrest et al. 2017; Zhou et al. 2020). Forrest et al. (2017) found a redshift peak at $z = 3.5$ with EELGs and SELGs in the ZFOURGE catalog. The seventh nearest-neighbor measure is used to build the overdensities projected on the sky, revealing the densest region of extreme [O III] emitters in ECDFS, with 53 member galaxies over a scale of 8.1 cMpc.

Maschietto et al. (2008) reported 13 [O III] emitters around the radio galaxy MRC 0316–257 at $z = 3.13$. This radio-selected protocluster consists of 32 LAEs over a $7' \times 7'$ region (Venemans et al. 2005). These 13 [O III] emitters form an overdensity with $\delta_{\text{gal}} \sim 2.5$. Kuiper et al. (2012) found that MRC 0316–257 has a foreground structure at $z = 3.10$ traced by three spectroscopically confirmed [O III] emitters. They pointed out that the two structures are unlikely part of a larger protocluster based on a two-dimensional Kolmogorov–Smirnov test. We identify two substructures in our $z = 3.25$ overdense structure traced by 34 [O III] ELGs in ECDFS. We lack spectroscopic redshifts to see whether the NW substructure is located at the same redshift as the SE substructure. From the spatial distribution of our 34 [O III] ELGs, the two substructures likely belong to the same large-scale structure.

A recent work from the VANDELS survey presented several overdensities traced by $\text{Ly}\alpha$ emitters at $2 < z < 4$ in CDFS and UDS (Guaita et al. 2020). We take their overdensities near $z = 3.25$ for a comparison. As shown in Figure 10, the central locations of three overdensities at $z = 3.17, 3.23, \text{ and } 3.29$ are overplotted in ECDFS. However, the spatial locations of the VANDELS $\text{Ly}\alpha$ overdensities are not exactly coincident with our SE and NW components. The spatial offsets between them could be explained by the systematic offsets between different populations from the density tracers, say, the [O III] and $\text{Ly}\alpha$ emitters. [O III] emitters are more massive and metal-rich, while the $\text{Ly}\alpha$ emitters are mostly low-mass and metal-poor. The typical present-day mass of the VANDELS overdensities is

about $0.3 \times 10^{13} M_{\odot}$, which is about a factor of two and three lower than our NW and SE components, respectively.

In addition, some of our sample [O III] ELGs exhibit significant dust attenuation and high SFR, compared to normal SFGs at the same redshifts. This hints that star formation and metal enrichment in this overdensity are enhanced. No detection of extreme [O III] ELGs ($\text{EW}([\text{O III}])_{\text{rest}} > 500 \text{ \AA}$) in this overdensity also supported the acceleration of galaxy evolution in the overdense environment, in which low-mass and low-metallicity starburst galaxies are deficient. However, protoclusters at similar redshifts have been found to have quiescent galaxies largely concentrated in the overdense region, probably due to the environmental quenching (Shi et al. 2021; McConachie et al. 2022). These hint that the evolutionary states of protoclusters largely decide the environmental impacts on the member galaxies at $z > 3$.

7. Summary and Conclusions


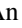
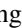
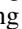



Using the deep narrowband H₂S(1) and broadband K_s imaging of ECFDS, we identify a sample of 34 [O III] ELGs at $z \sim 3.25$ and carry out an analysis of their physical properties. Using preexisting multiwavelength data, we construct SEDs from U to K_s and perform SED fitting with CIGALE to obtain rest-frame UVJ colors, stellar mass, SFR, dust attenuation, [O III] EW, and [O III] luminosities. The sample [O III] ELGs map an overdense structure that may be the progenitor of a Coma-like massive galaxy cluster at $z \sim 0$. Our main results are summarized as follows:

1. The vast majority of our sample are SFGs with strong [O III] emission lines. Compared with the extreme [O III] ELGs of $\text{EW}([\text{O III}])_{\text{rest}} > 500 \text{ \AA}$, our sample galaxies have $\text{EW}([\text{O III}])_{\text{rest}} \sim 70\text{--}500 \text{ \AA}$, are more massive with $M_{*} \sim 10^{9.0}\text{--}10^{10.6} M_{\odot}$, and have higher SFRs of $\sim 10\text{--}210 M_{\odot} \text{ yr}^{-1}$ compared to typical SFGs at the same masses. Only one target is identified as an AGN detected in the Chandra 7 Ms X-ray observations. According to the UVJ color–color diagram, the majority of our [O III] ELGs are located at the blue end of the star-forming regime. Our sample [O III] ELGs exhibit significant dust attenuation and high SFR compared to normal SFGs. Our results show that the NIR selection is able to pick a significant fraction of [O III] ELGs with high dust attenuation ($A_V > 1 \text{ mag}$), and our sample is more representative of the main population of SFGs at $z \sim 3\text{--}4$ in comparison with the extreme [O III] ELGs with $\text{EW}([\text{O III}])_{\text{rest}} > 500 \text{ \AA}$.
2. With HST/ACS and WFC3 observations we show that $z = 3.25$ [O III] ELGs have a variety of morphologies in the rest-frame UV and optical. We find that 38% (13/34) of our [O III] ELGs appear to have a diffuse/clumpy/tidal shape and about 35% (12/34) are very compact with $R_e < 0''.3$. Three [O III] ELGs are identified as mergers, and four are considered to be galaxy pairs with two galactic nuclei with similar color and size within a separation distance of $2''$. Two [O III] ELGs are too faint in the rest-frame UV to be recognized in morphology, likely due to heavy dust attenuation. And the large fraction of compact sources in our sample also tend to be located above the star formation main sequence of $z \sim 3$ SFGs.

3. We find that our [O III] ELGs trace an overdense structure at $z = 3.25$. This structure is composed of two substructures of scales of $5' \times 7'$ and $4.4' \times 4.4'$, separated by 21.8 cMpc. We take the half of narrowband filter redshift span as the upper limit and the minor axis of the three different overdensity rectangular areas as the lower limit for the line-of-sight comoving distance to estimate the number density per comoving volume. Our estimate suggests that this structure has an overdensity factor $\delta_{\text{gal}} \sim 9\text{--}12$ over a comoving volume of $25^3\text{--}23^3 \text{ cMpc}^3$. The SE and NW substructures are denser, with δ_{gal} in the range of 22–60 over a volume of $15^3\text{--}11^3 \text{ cMpc}^3$ and 18–57 over a volume of $12^3\text{--}8^3 \text{ cMpc}^3$, respectively. We estimate their present-day mass to be $\sim 1.1 \times 10^{15} M_{\odot}$ for SE and $\sim 4.8 \times 10^{14} M_{\odot}$ for NW, and these two substructures are likely to merge into a Coma-like massive cluster with $\sim 2.3 \times 10^{15} M_{\odot}$ at the present day.
4. We stress that none of our sample [O III] ELGs exhibit $\text{EW}([\text{O III}])_{\text{rest}} > 500 \text{ \AA}$. We argue that the lack of [O III] EELGs is largely due to our sample of [O III] ELGs residing in the overdense environment, in which star formation and chemical enrichment in galaxies are enhanced and low-mass and low-metallicity starburst galaxies are deficient.

This work is supported the National Science Foundation of China (12073078 and 12173088); the Major Science and Technology Project of Qinghai Province (2019-ZJ-A10); the science research grants from the China Manned Space Project with Nos. CMS-CSST-2021-A02, CMS-CSST-2021-A04, and CMS-CSST-2021-A07; and the Chinese Academy of Sciences (CAS) through a China-Chile Joint Research Fund (CCJRF No. 1809) administered by the CAS South America Centre for Astronomy (CASSACA). This research adopts data obtained through the Telescope Access Program (TAP), which is funded by the National Astronomical Observatories and the Special Fund for Astronomy from the Ministry of Finance.

ORCID iDs

Run Wen  <https://orcid.org/0000-0002-8705-6327>
 Fangxia An  <https://orcid.org/0000-0001-7943-0166>
 Xian Zhong Zheng  <https://orcid.org/0000-0003-3728-9912>
 Dong Dong Shi  <https://orcid.org/0000-0002-4314-5686>
 Jianbo Qin  <https://orcid.org/0000-0002-5179-1039>
 Valentino Gonzalez  <https://orcid.org/0000-0002-3120-0510>
 Fuyan Bian  <https://orcid.org/0000-0002-1620-0897>
 Haiguang Xu  <https://orcid.org/0000-0001-9405-0137>
 Zhizheng Pan  <https://orcid.org/0000-0001-5662-8217>
 Qing-Hua Tan  <https://orcid.org/0000-0003-3032-0948>
 Shuang Liu  <https://orcid.org/0000-0002-0623-4022>

References

- An, F., Zheng, X., Meng, Y., et al. 2013, *SCPMA*, 56, 2226
 An, F. X., Zheng, X. Z., Wang, W.-H., et al. 2014, *ApJ*, 784, 152
 Atek, H., Siana, B., Scarlata, C., et al. 2011, *ApJ*, 743, 121
 Barro, G., Faber, S. M., Koo, D. C., et al. 2017, *ApJ*, 840, 47
 Barrow, K. S. S., Robertson, B. E., Ellis, R. S., et al. 2020, *ApJL*, 902, L39
 Bertin, E., & Arnouts, S. 1996, *A&AS*, 117, 393
 Boquien, M., Burgarella, D., Roehlly, Y., et al. 2019, *A&A*, 622, A103
 Brammer, G. B., Sánchez-Janssen, R., Labbé, I., et al. 2012, *ApJL*, 758, L17
 Brammer, G. B., van Dokkum, P. G., & Coppi, P. 2008, *ApJ*, 686, 1503
 Brammer, G. B., Whitaker, K. E., van Dokkum, P. G., et al. 2011, *ApJ*, 739, 24
 Bruzual, G., & Charlot, S. 2003, *MNRAS*, 344, 1000

- Buat, V., Giovannoli, E., Heinis, S., et al. 2011, *A&A*, 533, A93
- Bunker, A. J., Warren, S. J., Hewett, P. C., & Clements, D. L. 1995, *MNRAS*, 273, 513
- Caldwell, J. A. R., McIntosh, D. H., Rix, H.-W., et al. 2008, *ApJS*, 174, 136
- Calzetti, D., Armus, L., Bohlin, R. C., et al. 2000, *ApJ*, 533, 682
- Cardamone, C., Schawinski, K., Sarzi, M., et al. 2009, *MNRAS*, 399, 1191
- Cardamone, C. N., van Dokkum, P. G., Urry, C. M., et al. 2010, *ApJS*, 189, 270
- Carnall, A. C., McLure, R. J., Dunlop, J. S., et al. 2019, *MNRAS*, 490, 417
- Chabrier, G. 2003, *PASP*, 115, 763
- Chiang, Y.-K., Overzier, R., & Gebhardt, K. 2013, *ApJ*, 779, 127
- Chiang, Y.-K., Overzier, R. A., Gebhardt, K., & Henriques, B. 2017, *ApJL*, 844, L23
- Cohn, J. H., Leja, J., Tran, K.-V. H., et al. 2018, *ApJ*, 869, 141
- Dale, D. A., Helou, G., Magdis, G. E., et al. 2014, *ApJ*, 784, 83
- De Barros, S., Oesch, P. A., Labbé, I., et al. 2019, *MNRAS*, 489, 2355
- de Barros, S., Schaerer, D., & Stark, D. P. 2014, *A&A*, 563, A81
- de Barros, S., Vanzella, E., Amorín, R., et al. 2016, *A&A*, 585, A51
- Du, X., Shapley, A. E., Tang, M., et al. 2020, *ApJ*, 890, 65
- Endsley, R., Stark, D. P., Chevallard, J., & Charlot, S. 2021, *MNRAS*, 500, 5229
- Fan, X., Carilli, C. L., & Keating, B. 2006, *ARA&A*, 44, 415
- Fletcher, T. J., Tang, M., Robertson, B. E., et al. 2019, *ApJ*, 878, 87
- Forrest, B., Tran, K.-V. H., Broussard, A., et al. 2017, *ApJL*, 838, L12
- Forrest, B., Tran, K.-V. H., Broussard, A., et al. 2018, *ApJ*, 863, 131
- Fritz, J., Franceschini, A., & Hatziminaoglou, E. 2006, *MNRAS*, 366, 767
- Gawiser, E., van Dokkum, P. G., Herrera, D., et al. 2006, *ApJS*, 162, 1
- Geach, J. E., Smail, I., Best, P. N., et al. 2008, *MNRAS*, 388, 1473
- Gillman, S., Swinbank, A. M., Tiley, A. L., et al. 2019, *MNRAS*, 486, 175
- Gong, Y., Cooray, A., Silva, M. B., et al. 2017, *ApJ*, 835, 273
- Gómez-Guijarro, C., Magdis, G. E., Valentino, F., et al. 2019, *ApJ*, 886, 88
- Grogin, N. A., Kocevski, D. D., Faber, S. M., et al. 2011, *ApJS*, 197, 35
- Guaita, L., Pompei, E., Castellano, M., et al. 2020, *A&A*, 640, A107
- Harikane, Y., Ouchi, M., Ono, Y., et al. 2019, *ApJ*, 883, 142
- Hopkins, A. M., & Beacom, J. F. 2006, *ApJ*, 651, 142
- Hsieh, B.-C., Wang, W.-H., Hsieh, C.-C., et al. 2012, *ApJS*, 203, 23
- Jaskot, A. E., & Oey, M. S. 2013, *ApJ*, 766, 91
- Kashikawa, N., Shimasaku, K., Matsuda, Y., et al. 2011, *ApJ*, 734, 119
- Kashino, D., Lilly, S. J., Silverman, J. D., et al. 2021, *ApJ*, 909, 213
- Katz, H., Ďurovčíková, D., Kimm, T., et al. 2020, *MNRAS*, 498, 164
- Kewley, L. J., & Ellison, S. L. 2008, *ApJ*, 681, 1183
- Kewley, L. J., Nicholls, D. C., & Sutherland, R. S. 2019, *ARA&A*, 57, 511
- Khostovan, A. A., Malhotra, S., Rhoads, J. E., et al. 2020, *MNRAS*, 493, 3966
- Khostovan, A. A., Sobral, D., Mobasher, B., et al. 2015, *MNRAS*, 452, 3948
- Khostovan, A. A., Sobral, D., Mobasher, B., et al. 2016, *MNRAS*, 463, 2363
- Koekemoer, A. M., Faber, S. M., Ferguson, H. C., et al. 2011, *ApJS*, 197, 36
- Kriek, M., Shapley, A. E., Reddy, N. A., et al. 2015, *ApJS*, 218, 15
- Kuiper, E., Venemans, B. P., Hatch, N. A., et al. 2012, *MNRAS*, 425, 801
- Lambrides, E. L., Chiaberge, M., Heckman, T., et al. 2020, *ApJ*, 897, 160
- Liu, S., Luo, A.-L., Yang, H., et al. 2022, *ApJ*, 927, 57
- Lumbreras-Calle, A., López-Sanjuan, C., Sobral, D., et al. 2021, arXiv:2112.06938
- Luo, B., Brandt, W. N., Xue, Y. Q., et al. 2017, *ApJS*, 228, 2
- Ly, C., Lee, J. C., Dale, D. A., et al. 2011, *ApJ*, 726, 109
- Madau, P., & Dickinson, M. 2014, *ARA&A*, 52, 415
- Maíz Apellániz, J. 2006, *AJ*, 131, 1184
- Mannucci, F., Cresci, G., Maiolino, R., Marconi, A., & Gnerucci, A. 2010, *MNRAS*, 408, 2115
- Maschietto, F., Hatch, N. A., Venemans, B. P., et al. 2008, *MNRAS*, 389, 1223
- Maseda, M. V., van der Wel, A., Rix, H.-W., et al. 2014, *ApJ*, 791, 17
- McConachie, I., Wilson, G., Forrest, B., et al. 2022, *ApJ*, 926, 37
- McLean, I. S., Steidel, C. C., Epps, H. W., et al. 2012, *Proc. SPIE*, 8446, 84460J
- McLinden, E. M., Finkelstein, S. L., Rhoads, J. E., et al. 2011, *ApJ*, 730, 136
- McLinden, E. M., Malhotra, S., Rhoads, J. E., et al. 2013, *ApJ*, 767, 48
- Meurer, G. R., Heckman, T. M., & Calzetti, D. 1999, *ApJ*, 521, 64
- Momcheva, I. G., Brammer, G. B., van Dokkum, P. G., et al. 2016, *ApJS*, 225, 27
- Nakajima, K., Ellis, R. S., Iwata, I., et al. 2016, *ApJL*, 831, L9
- Nakajima, K., Ellis, R. S., Robertson, B. E., Tang, M., & Stark, D. P. 2020, *ApJ*, 889, 161
- Nakajima, K., & Ouchi, M. 2014, *MNRAS*, 442, 900
- Nakajima, K., Ouchi, M., Shimasaku, K., et al. 2013, *ApJ*, 769, 3
- Noll, S., Burgarella, D., Giovannoli, E., et al. 2009, *A&A*, 507, 1793
- Noll, S., Pierini, D., Cimatti, A., et al. 2009, *A&A*, 499, 69
- Oke, J. B. 1974, *ApJS*, 27, 21
- Onodera, M., Carollo, C. M., Lilly, S., et al. 2016, *ApJ*, 822, 42
- Onodera, M., Shimakawa, R., Suzuki, T. L., et al. 2020, *ApJ*, 904, 180
- Price, S. H., Kriek, M., Barro, G., et al. 2020, *ApJ*, 894, 91
- Puget, P., Stadler, E., Doyon, R., et al. 2004, *Proc. SPIE*, 5492, 978
- Qin, J., Zheng, X. Z., Fang, M., et al. 2022, *MNRAS*, 511, 765
- Reddy, N. A., Shapley, A. E., Sanders, R. L., et al. 2018, *ApJ*, 869, 92
- Reddy, N. A., Steidel, C. C., Pettini, M., et al. 2008, *ApJS*, 175, 48
- Rix, H.-W., Barden, M., Beckwith, S. V. W., et al. 2004, *ApJS*, 152, 163
- Robertson, B. E., Ellis, R. S., Furlanetto, S. R., & Dunlop, J. S. 2015, *ApJL*, 802, L19
- Schenker, M. A., Ellis, R. S., Konidaris, N. P., & Stark, D. P. 2013, *ApJ*, 777, 67
- Shapley, A. E., Reddy, N. A., Kriek, M., et al. 2015, *ApJ*, 801, 88
- Shi, K., Toshikawa, J., Lee, K.-S., et al. 2021, *ApJ*, 911, 46
- Shivaei, I., Reddy, N., Rieke, G., et al. 2020, *ApJ*, 899, 117
- Skelton, R. E., Whitaker, K. E., Momcheva, I. G., et al. 2014, *ApJS*, 214, 24
- Sobral, D., Matthee, J., Best, P. N., et al. 2015, *MNRAS*, 451, 2303
- Sobral, D., Smail, I., Best, P. N., et al. 2013, *MNRAS*, 428, 1128
- Sommariva, V., Mannucci, F., Cresci, G., et al. 2012, *A&A*, 539, A136
- Steidel, C. C., Adelberger, K. L., Dickinson, M., et al. 1998, *ApJ*, 492, 428
- Steidel, C. C., Erb, D. K., Shapley, A. E., et al. 2010, *ApJ*, 717, 289
- Steidel, C. C., Rudie, G. C., Strom, A. L., et al. 2014, *ApJ*, 795, 165
- Straatman, C. M. S., Spitler, L. R., Quadri, R. F., et al. 2016, *ApJ*, 830, 51
- Straughn, A. N., Pirzkal, N., Meurer, G. R., et al. 2009, *AJ*, 138, 1022
- Suzuki, T. L., Kodama, T., Sobral, D., et al. 2016, *MNRAS*, 462, 181
- Suzuki, T. L., Kodama, T., Tadaki, K.-i., et al. 2015, *ApJ*, 806, 208
- Tang, M., Stark, D. P., Chevallard, J., & Charlot, S. 2019, *MNRAS*, 489, 2572
- Tang, M., Stark, D. P., Chevallard, J., et al. 2021a, *MNRAS*, 501, 3238
- Tang, M., Stark, D. P., Chevallard, J., et al. 2021b, *MNRAS*, 503, 4105
- Tang, M., Stark, D. P., & Ellis, R. S. 2022, *MNRAS*, 513, 5211
- Thomas, D., Maraston, C., Bender, R., & Mendes de Oliveira, C. 2005, *ApJ*, 621, 673
- Tomczak, A. R., Quadri, R. F., Tran, K.-V. H., et al. 2016, *ApJ*, 817, 118
- Tran, K.-V. H., Forrest, B., Alcorn, L. Y., et al. 2020, *ApJ*, 898, 45
- Truncoso, P., Maiolino, R., Sommariva, V., et al. 2014, *A&A*, 563, A58
- Venemans, B. P., Röttgering, H. J. A., Miley, G. K., et al. 2005, *A&A*, 431, 793
- Villa-Vélez, J. A., Buat, V., Theulé, P., Boquien, M., & Burgarella, D. 2021, *A&A*, 654, A153
- Wang, X., Li, Z., Cai, Z., et al. 2022, *ApJ*, 926, 70
- Weaver, J. R., Kauffmann, O. B., Ilbert, O., et al. 2022, *ApJS*, 258, 11
- Whitaker, K. E., Labbé, I., van Dokkum, P. G., et al. 2011, *ApJ*, 735, 86
- Wild, V., Charlot, S., Brinchmann, J., et al. 2011, *MNRAS*, 417, 1760
- Williams, R. J., Quadri, R. F., Franx, M., van Dokkum, P., & Labbé, I. 2009, *ApJ*, 691, 1879
- Worseck, G., Prochaska, J. X., O'Meara, J. M., et al. 2014, *MNRAS*, 445, 1745
- Yang, H., Malhotra, S., Gronke, M., et al. 2017, *ApJ*, 844, 171
- Yates, R. M., Schady, P., Chen, T.-W., Schweyer, T., & Wiseman, P. 2020, *A&A*, 634, A107
- Yuan, F.-T., Burgarella, D., Corre, D., et al. 2019, *A&A*, 631, A123
- Yuma, S., Ouchi, M., Fujimoto, S., Kojima, T., & Sugahara, Y. 2019, *ApJ*, 882, 17
- Zhai, Z., Wang, Y., Benson, A., Chuang, C.-H., & Yepes, G. 2021, *MNRAS*, 505, 2784
- Zheng, X. Z., Cai, Z., An, F. X., Fan, X., & Shi, D. D. 2021, *MNRAS*, 500, 4354
- Zhou, L., Elbaz, D., Franco, M., et al. 2020, *A&A*, 642, A155